Spring 2009

Applied electrokinetics for tissue engineering applications

Stephanie R. Tully-Dartez
Louisiana Tech University

APPLIED ELECTROKINETICS FOR TISSUE ENGINEERING APPLICATIONS

by

Stephanie R. Tully- Dartez, B.S.

A Dissertation Presented in Partial Fulfillment
of the Requirements for the Degree
Doctor of Philosophy

COLLEGE OF ENGINEERING AND SCIENCE
LOUISIANA TECH UNIVERSITY

May 2009

UMI Number: 3358245

INFORMATION TO USERS

The quality of this reproduction is dependent upon the quality of the copy submitted. Broken or indistinct print, colored or poor quality illustrations and photographs, print bleed-through, substandard margins, and improper alignment can adversely affect reproduction.

In the unlikely event that the author did not send a complete manuscript and there are missing pages, these will be noted. Also, if unauthorized copyright material had to be removed, a note will indicate the deletion.

UMI®

LOUISIANA TECH UNIVERSITY

THE GRADUATE SCHOOL
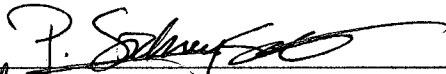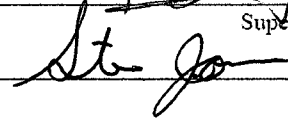
4/14/09
Date

We hereby recommend that the dissertation prepared under our supervision

by Stephanie R. Tully–Dartez

entitled Applied Electrokinetics for Tissue Engineering Applications

be accepted in partial fulfillment of the requirements for the Degree of Doctorate of Philosophy in Biomedical Engineering

Supervisor of Dissertation Research

Head of Department

Department

Recommendation concurred in:
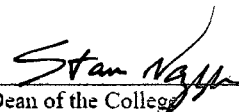
Advisory Committee

Approved:

Director of Graduate Studies

Dean of the College

Approved:

Dean of the Graduate School

ABSTRACT

Tissue engineering could provide an alternative source of transplant tissue regardless of donor supply and with reduced risk of immune rejection. Engineered tissue requires three critical components for successful development: the cells, growth factors, and the scaffold on which they will initially grow. The scaffold acts as a temporary extra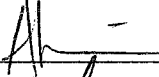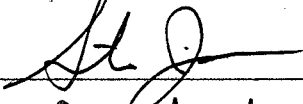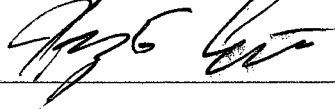cellular matrix (ECM) allowing cell attachment and acclimation to the environment prior to synthesis and construction of the cell's native ECM. Prior to cell seeding, the scaffold must be characterized to determine whether or not the pore geometry is conducive to cell implantation. Electrochemical impedance spectroscopy (EIS) provides a unique and effective tool for scaffold evaluation upon fabrication as well as following modification and cell seeding. Chitosan scaffolds were tested with EIS showing good comparative values to more common and proven characterization methods.
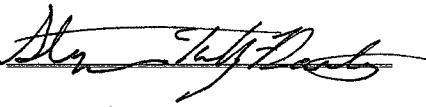
In addition to characterization, modification may be necessary to improve the cell scaffold interaction. Previous attempts to modify chitosan scaffolds with microparticles during the fabrication have shown that these approaches compromise scaffold integrity; however, particles cannot be effectively forced into the scaffold without damaging it. In light of this difficult modification, electrophoretic particle treatment was implemented. Transport of iron oxide microparticles at low voltage was proven an effective modification method and might be capable of modifying a seeded scaffold.

Finally, it is necessary to not only evaluate the scaffold prior to cell seeding but also subsequent to cell seeding. Successful seeding should lead to cellular proliferation, gene expression, and ECM production. EIS has become a common tool for tissue characterization and can, in turn, be used as an evaluative approach for the assessment of engineered tissues. While cell response and volume exclusion requires a large quantity of cells, varying protein concentrations were notable in scaffolds saturated with complete cell media. In summary, electrokinetics has shown its potential for tissue engineering applications from scaffold fabrication to online monitoring.

APPROVAL FOR SCHOLARLY DISSEMINATION

The author grants to the Prescott Memorial Library of Louisiana Tech University the right to reproduce, by appropriate methods, upon request, any or all portions of this Dissertation. It is understood that "proper request" consists of the agreement, on the part of the requesting party, that said reproduction is for his personal use and that subsequent reproduction will not occur without written approval of the author of this Dissertation. Further, any portions of the Dissertation used in books, papers, and other works must be appropriately referenced to this Dissertation.

Finally, the author of this Dissertation reserves the right to publish freely, in the literature, at any time, any or all portions of this Dissertation.

Author _____

Date _____4/29/09_____

DEDICATION

To

My family and my husband, Shawn, for their continued support and encouragement and

to Mr. Kuhnell for never letting me settle for less than my best.

TABLE OF CONTENTS

LIST OF TABLES

LIST OF FIGURES

ACKNOWLEDGEMENTS

CHAPTER 1

INTRODUCTION

The need for suitable organ and tissue donors in the United States far exceeds the number available for transplant [1]. Those who receive transplants are at significant risk of graft rejection depending on the source of the transplant as well as the health of the recipient [2]. The mechanism by which the body rejects the donor graft is through identification of the major histocompatibility complex (MHC) on the donor cell surface by the recipient's immune system. Consequently, the optimal donors for tissue are the recipients themselves, an immediate family member, or a donor with similar MHC. These types of grafts are known as autografts and allografts respectively. Alternatively, xenograft tissue could be acquired from another species. In the case of either an allograft or a xenograft, immunosuppressant drugs are given to the transplant recipient in order to prevent rejection. These drugs, which are intended to compromise the immune system, can leave the recipient susceptible to infection [3]. Because the benefits of autografts are substantial, an ideal strategy is to generate functional tissue from cells harvested from the patient. However, to promote the cells to interact properly and to express the correct phenotype, it is necessary to provide them with an appropriate chemical, geometrical and mechanical environment. Consequently, it is important to have techniques that can accurately evaluate the properties of materials (scaffolds) that support the cells during

their development. Therefore, this dissertation examines one such tool, electrokinetics, and evaluates its ability to characterize properties of a biomaterial scaffold.

1.1 Tissue Engineering Requirements

Due to the incredible need for donor organs and tissue as well as the difficulty in procurement and compatibility, an alternative source of organs or tissues must be identified. Tissue engineering could provide such an alternative source of transplant tissue regardless of donor supply and with reduced risk of immune rejection.

Engineered tissue requires three critical components for successful development: cells, growth factors, and the scaffold on which they will initially grow. The acquisition of cells from the graft recipient allows for a small collection of cells to be cultured and proliferated. Also, the use of cells from the recipient reduces the risk of rejection to virtually zero [4]. Therefore, with the addition of an appropriate scaffold, engineered tissues from the recipient's cells remove both the compatibility issue as well as the need for external procurement.

The scaffold acts as a temporary extracellular matrix (ECM) allowing cell attachment and acclimation to the environment prior to synthesis and construction of the cell's native ECM at which point the scaffold would either degrade or be removed. In order to accommodate its function, the scaffold must be biocompatible both as a whole and upon degradation. The internal pore geometry must be accessible for cell infiltration but each pore must be an appropriate compartment size adequately large enough for the cells to enter but small enough to retain cells in close enough proximity for communication. The scaffold pore interconnectivity must facilitate the flow of nutrients in and waste out without disrupting cell attachment. Also, the scaffold material must be

durable and flexible enough to both modify the shape for the application and also withstand the mechanics of the grafting position [5]. In light of these requirements for scaffold production, scaffold characterization, modification, and evaluation would be best fitted within the dictates of scaffold structure parameters as well.

1.2 Scaffold Characterization

For successful implementation of a tissue engineered scaffold, it is important that the pore geometry not only be appropriately designed but also characterized following fabrication. There are several commonly used tools for the characterization of pore structure and porosity such as scanning electron microscopy (SEM), mercury intrusion porosimetry (MIP), gas adsorption, magnetic resonance imaging (MRI), and X-ray microtomography (μCT) [6-8].

SEM provides a 2D visualization of the surface while MRI and μCT use stacked images to provide a 3D model of the scaffold. Of the three visual methods, μCT can be performed under the most physiologically reasonable condition since it can be performed at full saturation although radiation is required [9]. While qualitative evaluation through visualization of the pore structure is helpful for novel scaffold designs, quality assurance could be better met using a method that provides a quantitative porosity.

Alternatively, the characterization data acquired from MIP utilizes non-wetting liquid mercury to fill the pore volume. MIP has demonstrated an effective detective of pore sizes in the range of approximately 3.6 nm to 200 μm plus [10]. Previous use of MIP for the characterization of tissue engineering scaffolds required freeze drying prior to testing and the discarding of the scaffold due to the presence of heavy metal [10]. Gas

adsorption involves nonabsorbable gases such as helium and surface deposition to provide porosity and pore diameter values for the scaffold [9].

Both of these methods are effective determiners of porosity but they are also time consuming and result is destruction of the test scaffold. A more useful characterization would be one that provides information about the pore geometry non-destructively and in a faster paced time frame. A nondestructive porosity test similar to MIP without the toxic contamination utilizes nitrogen with saturated scaffolds. Nitrogen is incrementally introduced at ever increasing pressure while the nature and degree of bubbling can be interpreted as pore size [9]. While this approach may provide data and still allow the reuse of the scaffold, the pressure applied would prohibit testing if particles or cells had been introduced into the system due to the potential for expulsion of these modifications under pressure. In lieu of the common characterization method limitations, the technique of electrochemical impedance spectroscopy (EIS), commonly used in geophysics and civil engineering, shall be compared to tested modes such as MIP.

1.3 Scaffold Modification

Scaffolds have been made of a variety of organic and inorganic materials with a range of properties that match the needs for engineered tissue [11, 12]. Some sample materials for scaffold fabrication include polylactic acid (PLA), polyglycolic acid (PGA), and collagen. Polymer based scaffolds have been generated from polymeric subunits which dictate subsequent scaffold strength and application. For polymer based scaffolds the degree of crosslinking determines the porosity and pore size as well as mechanical strength [13, 14]. Inorganic scaffolds for hard tissue replacement having been successfully generated with naturally occurring bone minerals such as hydroxyapatite via

electrodeposition [15]. Other hard tissues have been developed from ceramic scaffolds whose properties are determined upon manufacturing.

Beyond the properties rendered during scaffold production, it may also be necessary to modify the scaffold in order to readily facilitate cellular adhesion, proliferation, and differentiation. Scaffolds may be coated with proteins or other growth factors to encourage cellular growth or for some scaffold materials incorporated during fabrication. Vascular endothelial growth factor has previously been incorporated into poly lactic-co-glycolic acid (PLGA) scaffolds effectively increasing proliferation [16]. Another modification during fabrication was the encasement of bone morphogenic protein into composite scaffolds resulting in cellular osteoinduction [17].

Unlike those previously discussed, some scaffolding materials will not properly form if its chemical bonding is prevented by the introduction of modifying substances. If the scaffold is stable under pressure, modifying particles can be introduced via solution forced under pressure. A somewhat less destructive method for modification is plasma surface modification which can include physical alteration as well as chemical alteration. Surface etching can provide physical guides for structured cell growth [18]. While plasma modification is less likely to damage the scaffold structurally, it can not be used once cells are seeded in the scaffold due to physiological limitations.

Given the limitations of currently used methods, an alternative modification approach will be utilized for tissue engineering scaffolds. Once again, a technique more common to mechanical and civil engineering than tissue engineering will be attempted in order to modify the scaffold. Electrophoresis, a novel approach to scaffold modification,

will be used to incorporate particles into the porous substrate where their distribution will be qualitatively assessed.

1.4 Cell Monitoring

Once the cells have been incorporated into the scaffold, their distribution and status should be evaluated periodically to determine the functionality of the engineered tissue. The most common method for this evaluation is histological sampling of the engineered tissue. Slicing the sample and staining for both cell type and products of gene expression allows visualization of the tissue status [19, 20]. In PLGA scaffolds seeded with mesenchymal stem cells, staining for differentiated cells and for type II cartilage showed the cellular differentiation and tissue evolution over time [21]. Histological staining can also be accomplished with transmission electron microscopy [22]. While visual assessment of engineered tissues provides clear delineation among the cell types and expressed molecules, continuous non destructive evaluation throughout the life cycle of the graft is also necessary. On-line or continuous monitoring has been achieved with some engineered tissues using fluorescent indicators incorporated into the scaffold. As the scaffold degrades and the cells proliferate and the signal is muffled [23]. Microdialysis has also been used for on-line engineered tissue monitoring. Samples of the scaffold's physiological fluid are drawn through a capillary tube and sampled for molecules expressed from the cell [24]. Methods such as these are nondestructive but they do not truly provide information regarding cell number and distribution like the destructive histological analysis. Since EIS has previously been used in this experimental set for scaffold characterization, the approach will be used on seeded scaffolds as well.

The EIS technique has been chosen not only for its porous substrate characterization abilities but also its biological tissue characterization advantages.

1.5 Electrokinetics in Tissue Engineering

Characterization, modification, and evaluation of engineered tissues have often led to their destruction or reduced functionality. The goal of this experimental set was to demonstrate the effectiveness of EIS for characterizing pore geometry and chitosan scaffolds quickly and nondestructively. Additionally, the effectiveness of particle modification via electrophoresis was evaluated and finally EIS was once again utilized as an on-line monitoring application for scaffolds seeded with NIH 3T3 fibroblasts. The material chosen was chitosan, a naturally occurring polysaccharide that readily forms a regular porous matrix but is often unstable if modified during fabrication. Chitosan scaffolds are also flexible which makes chitosan a good choice for fitting into defects but not stable enough for excessive handling [25]. In total, an alternative non destructive approach for characterization, modification, and evaluation would be both necessary given its limitations and useful due to the vulnerability of the scaffold structures. The summation of the chitosan model experimental set should encapsulate the overall usefulness of electrokinetics in tissue engineering.

Following this introductory chapter is Chapter 2 which covers the background and literature review of chitosan, EIS, current flow in a porous substrates, and electrical current effect on biological tissue. Chapter 3 discusses the experimental evaluation of EIS as a characterization method for chitosan scaffolds. In Chapter 4, the electrophoretic deposition of particles into chitosan scaffolds will be detailed and, in Chapter 5, EIS applications for seeded cell scaffolds will be discussed. In summary, Chapter 6 will

cover the significance of each of the three distinct experiments, how they relate to each other, and the future work associated with these results.

CHAPTER 2

BACKGROUND AND THEORY

2.1 Chitosan

Chitosan is the product of the deacetylation of the nonpolar glucose derivative

chitin. The deacetylation converts the chitin non polar end group to an amino group

which naturally has an acid dissociation constant around 6.5 (Figure 1). While the chain

lengths are somewhat variable, the percentage of deacetylation has the greatest effect on

crystallinity with increased deacetylation leading to a stronger structure *in vivo* [26].

These amino end groups provide a charge and allow for the dissolution of the chitosan in

a neutral or slightly acidic aqueous solvent. For scaffold formation, the chitosan is

dissolved in the solvent between 1% and 3% weight per volume (wt/vol) for practical

tissue engineering applications. Scaffold properties and stability depend on the

percentage used with increased percentage resulting in a decreased pore size [27].
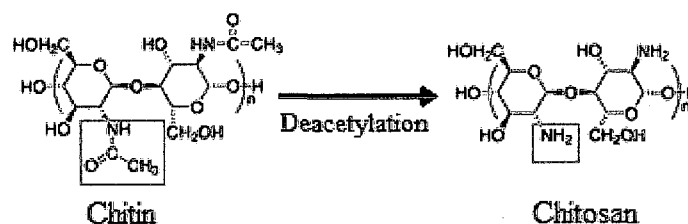
Figure 1: Chemical structure of chitin and its deacetylation product, chitosan [26].

Once completely dissolved, the chitosan in solution is thoroughly frozen. The speed of the freezing has an effect on the chitosan properties. During freezing, microscopic ice crystals form and force the chitosan out. These micro sized ice crystals each become individually surrounded by the polar chitosan salt which forms a partial shell around the crystal. Thorough and even temperature freezing insures even crystal sizes throughout the scaffold and thus uniform pore sizes and distribution. Freeze drying the scaffold causes the ice crystals to sublimate leaving behind voids or pores in their place [28]. While kept dry, the scaffold is stable at room temperature.

Previous characterizations of chitosan scaffolds have revealed an evenly distributed pore structure with pores ranging for 500 μm for low concentration scaffolds to 50 μm for higher concentrations. The degree of deacetylation has a significant effect on pore size as well solid scaffold volume. With deacetylation levels of 88% and higher, the resulting pore diameters are less than 100 μm and have low lateral pore connectivity. These variations are caused by the shift in chitosan molecule shapes due to the exposure of charged amino sites. With greater deacetylation, the charged groups cause the molecule to straighten [29, 30]. Microscopy of scaffold cross-sections has shown that pores are consistently spherical, so the number and size of the pores dictate the pore interconnectivity.

Chitosan scaffolds have demonstrated great potential for tissue engineering because of their unique naturally occurring properties. Chitosan scaffolds implanted in mice show no sign of an inflammatory response. Neutrophil presence is detected in the early implantation stage but quickly fades over time. The natural antimicrobial nature of chitosan has shown that even *in vivo* infection is inhibited. Over time, connective tissue

from the recipient's body has shown infiltration into the scaffold which demonstrates not only biocompatibility but also bio-inertness. In addition to connective tissue, angiogenesis has been noted on the scaffold surface [31].

Studies of cell seeding in chitosan scaffolds have shown good retention rates. The surface charge of the scaffold encourages cellular attachment along the chitosan [32]. Previously presented data has suggested that ~31% of chondrocytes introduced into the scaffold will successfully integrate into the scaffold. With pores in the 100-200 μm range, cells were not only seeded throughout the scaffold but also produced extracellular matrix components which eventually replaced the scaffold as it degrades. Morphology and expression of the cells in chitosan scaffolds remains typical of the phenotype, further demonstrating its effectiveness as a tissue engineering scaffold [32]. Other studies have also shown the strong potential of chitosan for the development of cartilaginous tissue and hard tissue [33-35]. Finally, chitosan degradation rates correspond to both the original structure of the scaffold prior to implantation but also to the implantation site environment. The products of this degradation are sugars and can be easily removed by the body itself [36].

Many attempts to modify 2D chitosan films have been successful but modification of the 3D chitosan scaffolds has been less frequently documented. One example is the binding of RGD (Arg–Gly–Asp–Ser) for increased biocompatibility to chitosan scaffolds. In the case of small amino groups, the scaffold can be dipped into a suspension and the charges will initiate the immobilization [37]. Glycoconjugates have been immobilized by similar methods but as before the molecules are on the nanoscale [6]. Alternatively, composite scaffolds can be made by incorporating other structural

particles such as gelatin and cartilage during fabrication however this varies the mechanism of pore formation and the structures themselves [38]. In order to keep the same pore formation and regularity; modification must be made subsequent to lyophilization. Attempts to modify with nanoparticles have been successful as previously described but larger particles fail to infiltrate the inner areas of a complete scaffold without pressurization [39].

2.2 Electrochemical Impedance Spectroscopy (EIS)

Electrical resistance is the resistance of current flow through a material described in Ohm's law as the voltage divided by the current. This simple equation only applies to direct current or to an ideal scenario when alternating currents are completely in phase. Realistically, materials with applied AC voltage will not have a simple resistance but rather complex impedance. Complex impedance ($\widetilde{Z}$) can be defined as the drop in voltage over a current while taking into account the frequency response and the lag of the phase:

$$\widetilde{Z} = Z e^{j\theta}, \tag{2.1}$$

where Z is the ratio of the voltage difference to the current, θ is the phase lag (Figure 2), and j is the imaginary unit. Alternatively, complex impedance can be viewed in terms of the real and imaginary components:

$$\widetilde{Z} = R + jX , \tag{2.2}$$

where the real component (R) is the resistance and the imaginary component (X) is the reactance resulting from the accumulation of electric fields which also inhibit current flow [40].
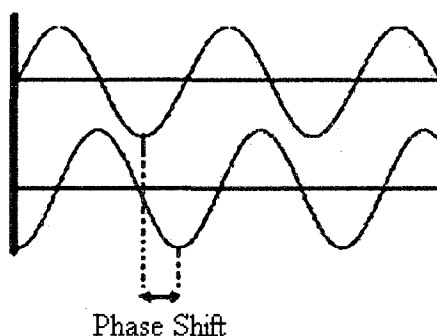
Phase Shift

Figure 2: Phase shift showing lag in the signal over time (x axis).

In EIS, the real and imaginary components not only provide electrical information about the material in question but also about the geometric structures inside. EIS requires the use of two to four electrodes which transmit a weak current through the sample in question. As long as the sample is conductive, current will pass between the electrodes via the path of least resistance. In a nonconductive porous substrate, this path is through the conductive pore fluid. The input AC signal varies over a set frequency range from highest to lowest and the response to the test material is recorded at each frequency value. The complex impedance can be plotted as a vector product of both the real and imaginary components of impedance with the angle being the phase (Figure 3).
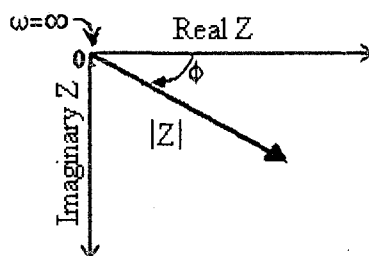
Figure 3: Complex impedance magnitude shown as a vector product of the real and imaginary impedance.

The vector relationship allows for data points from an EIS frequency sweep to be plotted as a Nyquist plot of the real and imaginary impedance as the X and Y values, respectively. The characteristic curve or curves are indicative of the resistance properties of the material. In order to note frequency response, Bode plots can also be constructed from EIS data as well. Bode plots can be created using the log of the impedance magnitude or the phase shift angle versus the log of the frequency. Both options denote frequency dependent changes and indicate whether or not the system has a single time constant. The use of Nyquist and Bode plots are common practice in EIS analysis and can be used to produce an equivalent circuit.

Equivalent circuits are used to model the impedance values for a material using classical circuit elements. Of course, complex impedance necessitates a minimum of both a resistive element and a capacitive element but the total number and strength of each is based on the contributing factors in the modeled material. For example, a coated substrate would have a capacitor and a resistor associated with the substrate but also circuit elements associated with the coating. Resistor values can be estimated from Nyquist plots and the model values are typically tested with a circuit simulation program [41].

For a nonconductive porous substrate, the bulk resistivity as determined by the Nyquist plot is essentially the cumulative resistance to current flow through the conductive media. This resistance is the electrical analog to the physical resistance to flow within the system and can lead to the estimation of porosity. By taking the bulk resistivity and converting it to conductivity, the conductivity of the system is related to

the conductivity of the pore fluid based on the pore volume of the system and can be interpreted through Archie's Law as porosity

$$\Phi = \log\left(\frac{C_w S_w^n}{C_t}\right) / m, \qquad [2.3]$$

where Φ is the porosity, C_t is the substrate conductivity, C_w is the media conductivity, S_w is the unitless assessment of media saturation, m is the cementation exponent and n is the saturation exponent [42, 43]. The form of Archie's law will be discussed below in terms of individual applications.

2.3 Charge Flow Through a Porous Substrate

Current flows through a conductive media because charge carriers move under the motivation of an electric field. The charge carrier mobility (μ) is the velocity of the particle divided by the electric field strength which causes it to move. In the context of a non conductive porous system filled with a conductive fluid, internal geometry must be taken into account when considering current flow through the system. By considering the charge carriers to be confined to a finite space such as a column, the current can be defined in terms of the space and charge carrier concentration [44].

A column has a volume (*vol*) which is the product of the length multiplied by the area (*A*) of its circular base. In this case, the base will be a set value and the length will be defined as the change in position. With a known average particle velocity (*v*), the position (ΔX) can be defined as the product of velocity and the change in time (Δt)

$$vol = Av\Delta t = A\Delta X. \qquad [2.4]$$

If that volume is assumed to contain a specific number of charge carriers (*n*) each with a uniform charge (*q*) then the charge per volume (Δq) can be established

$$\Delta q = Aqnv\Delta t = Aqn\Delta X. \tag{2.5}$$

Since current, I, can be designated as the flow of charge, current can be defined as:

$$I = \frac{\Delta q}{\Delta t} = Aqnv. \tag{2.6}$$

In turn, the current density, J, which will remain the same throughout the geometry is the current divided by area

$$J = qnv. \tag{2.7}$$

In many porous systems, this model would apply directly; however, in a porous substrate with spherical pores, the volume can not be simply viewed as a cylinder with a standard cross sectional area but is rather dependent both on the pore diameter and porosity. Increased pore diameter does not necessarily mean increased charge carrier transport. Mobility inside the pores may be high but movement between the pores is limited by the diameter of the junction. With an increase in porosity comes an increase in pore connectivity.

With a constant pore size, the pores become closer together as the porosity increases leading to the creation of connections with circular cross sections (Figure 4). The circular cross section diameter increases with increased porosity. With regular pore size and connectivity, the connections are also regular and charge carrier transport through the connections can be assessed as a series of tubes with diameters equivalent to pore overlap. It is important to note that the spherical pore structure will play an important role when defining the relationship between electrical information and scaffold structure [45].

Increasing Porosity

Increasing Connectivity
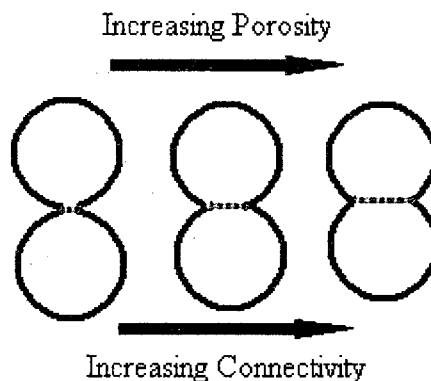
Figure 4: Representation of pore connections based on uniform spherical pores with increasing porosity and increasing connectivity (pore connections denoted as grey dashed line).

Electro-osmotic flow can be initiated in porous substrates with narrow pore networks. A double layer of ions from the solution forms along the walls in response to charge of the ions. The voltage potential across the substrate causes the positively charged ions to move in the direction of the negative electrode. As the positive ions move, they pull the water molecules with them. In a narrow tube, these pulled water molecules initiate a notable flow. In larger micron sized pore connections, the electro-osmotic flow will be negligible [46].

The addition of charged particles in a suspension of fluid influenced by an electric field can initiate travel in those particles. Electrical opposites attract so negatively charged particles are drawn toward the positive electrode and vice versa. If the electrostatic pull on the particle exceeds the friction force on the particle surface, the particle moves toward the electrode by means of electrophoresis. When particles are allowed to collect on the electrode, the process is referred to as electrodeposition. Charge carrier mobility is denoted as the velocity over the electric field, the mobility of particles

in solution is as the particle velocity over the electric field. Alternatively, particle mobility was also defined in terms of the surrounding media

$$\mu_e = v/E = \frac{\varepsilon \varepsilon_0 \zeta}{\eta},$$ [2.8]

where ε is the dielectric constant of the media, ε_0 is the permittivity of free space, η is the viscosity of the media, and ζ is zeta potential [47].

2.4 Current Effect on Biological Elements

Biological macromolecules and cellular components have unique and varying electrical properties. Tissue components can vary in response to electrical stimuli as a function of cell lineage, cell health, and even temperature [48]. Cell membranes are phospholipids bilayers which, by themselves, are electrically insulated. The integrated ion channels, which vary in number between cell types, add to the cells electrical properties by being gaps in the membrane insulation. In DC voltage, the bilayer can lead to flattening of the membrane as a result of increased hydrophobicity [49].

Intracellular components are also subject to electric field influence. Actin filaments and Golgi apparati have demonstrated elongation and movement along an electric field with the leading edge going toward the cathode. The applied voltage of 300 mV/mm caused not only the Golgi polarization but also resulted in cellular migration in the direction of the electric field [50]. Outside of the cell, extracellular matrix materials are also subject to current induced changes. Collagen type I monomers have increased fibrillogenesis when subjected to a voltage potential [51]. All of these biological changes result from modification of inherent charges.

While DC voltage has a notable affect on biological macromolecules, the influence of frequency from AC is more varied and notable. For example, the insulative phospholipid bilayer surrounds a conductive fluid and exists inside a conductive fluid so applied current will often have a capacitor like effect on the cell [52]. There are three frequency ranges of biological influence known as the α, β, γ dispersions (Table 1).

Table 1: Dispersion Frquencies for Biological Tissues.

Dispersion	Range
α	< 1000 Hz
β	1000 Hz < β < 100 kHz
γ	>100 kHz

The α dispersion primarily affects the ionic diffusion as previously discussed. The β dispersion is of primary importance for both the individual cell and tissue as a whole because of the cells dielectric response. Prior to the lower β values, the resistance of the system as a whole dominates and prevents the current from charging the cellular capacitors. Frequencies above the β dispersion go beyond the capacitive cellular reaction and initiate dipolar moments in other biological macromolecules such as proteins [53].

The variable frequency response of biological molecules and cells makes the use of EIS in tissue an effective tool for cellular and tissue characterization. Cell membranes have previously been noted for having a capacitive effect but in EIS each cell can be viewed as a two capacitor element (Figure 5).
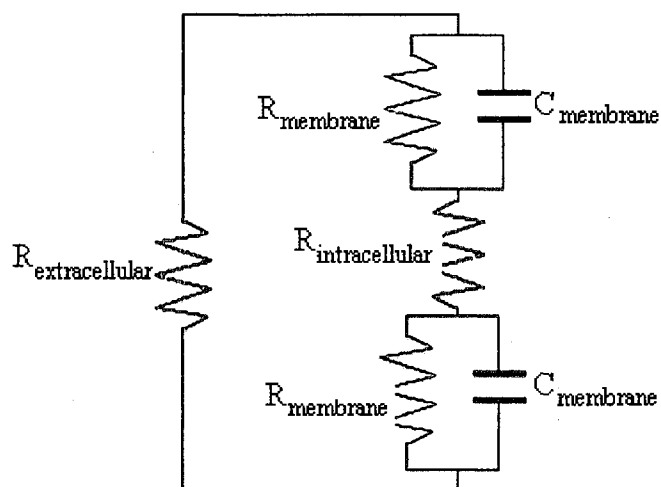
Figure 5: Standard model circuit of tissue [54]

A capacitor in circuit design is two parallel conductors separated by a non conductive dielectric. In cells, the phospholipid membrane is the non conductive dielectric. The membrane lies between the extracellular and intracellular fluid and, while different in ionic composition, both are conductive. This conductive/dielectric/conductive scenario accounts for the capacitive effect of the cell. In addition, the cell can be modeled as having two mirrored capacitors because of the parallel membrane sides. The integrated proteins which serve as ion channels can not be disregarded because these portals will allow the conduction of the current through the membrane so they must be counted as resistive elements [54]. Some cells have far more ion channels than others and the EIS data reflects this.

Since it has previously been established that the extracellular fluid is conductive, it can be understood that at low frequencies current will not enter the cell but will rather go around the cell through the conductive fluid. In this case, EIS in the alpha range will

suggest that the cell is simply a non conductive barrier in a conductive solution. The results will then be indicative of a primarily resistive scenario. At higher frequencies in the β dispersion, the capacitive effect will be initiated and a secondary impedance data set can be collected. Both of these frequency sets provide information regarding the nature and well being of the tissue in question.

In the α dispersion range, an increase in impedance over several days could be viewed as an increasing cellular population. As the number of cells increase, the volume of extracellular fluid accessible to the current would decrease. For clinical applications, an increase in impedance in lower frequencies is often indicative of ischemia where the cell membrane can't prevent the entrance of more fluid therefore causing an increased cell volume. Alternatively, a decrease in impedance can be seen as the compromising of the cell walls reducing the overall cell volume in the tissue and subtly increasing the extracellular volume.

In the β dispersion, the current passes not only around the cells but also through them adding a capacitive effect to EIS data collected. While in the α dispersion range, variation in cell quantity can be noted, the β frequencies can elucidate the variations among cell membrane behavior and the amount of extracellular fluid [55]. Cells of different phenotypes will not only present different morphologies but also vary in the number of gap junctions and ion channels depending on function. For example, cardiomyocytes have a greater number of gap junctions on their membrane than lung epithelial cells. Even with an overall identical cell population volume they will present different impedance values in response to β dispersion stimuli. The development of a library of reference impedance data dependent on cell type and viability allows for the

assessment of tissue through EIS on a set frequency range [54]. Previous studies have demonstrated that the tissue characterization abilities of EIS have potential for evaluating engineered tissues as well [56-58].

CHAPTER 3

PORE CHARACTERISTICS OF CHITOSAN SCAFFOLDS STUDIES BY ELECTROCHEMICAL IMPEDANCE SPECTROSCOPY

Manuscript Submitted to Tissue Engineering: Part C

3.1 Introduction

In the United States, thousands of individuals are in critical need of an organ or tissue transplant and many of those will not be matched with a suitable donor [1, 59-61]. Due to the incredible need for donor organs and tissue as well as the difficulty in procurement and compatibility, tissue engineering could provide an alternative source of transplant tissue with reduced risk of immune rejection [59-61]. The engineering of tissue requires three critical components: the cells, growth factors, and the scaffold on which the cells will initially grow. The scaffold acts as a temporary extracellular matrix (ECM) allowing cell attachment and acclimation to the environment. In order to accommodate its function, the scaffold must have several standard characteristics including biocompatibility of the scaffold as a whole as well as degradation byproducts, regular and cell accessible pore structure, and finally a means of or a naturally occurring degradation at an appropriate length of time [5].

To accommodate the cell infiltration into the scaffolds, the pore diameter must be large enough for the cells to enter and to pass through. At the same time, the porosity and interconnectivity of the pores must be high enough that cells will be well distributed throughout the scaffold. However, the pore diameter can not be so great that fluid flow throughout the scaffold interrupts cell attachment [5].

Due to the pore requirements for the successful implementation of tissue engineered scaffold, it is important to not only appropriately design a scaffold but also evaluate its structure upon fabrication. There are several methods for determining pore structure and porosity such as scanning electron microscopy (SEM), mercury intrusion (MIP) [10], gas adsorption, and X-ray microtomography (μCT) [9]; however, these methods all have distinctive drawbacks which can prevent continued evaluation of the scaffold. SEM can provide visualization of the pore geometry and allow for diameter determination but it also requires cutting of the dried sample, sputtering with gold, and exposure to high vacuum. Similarly, MIP can be used to determine porosity and interpret pore size. A vacuum operating condition is required in order to force mercury into the pores of the dried sample and therefore the sample is consumed. For gas adsorption, once again, vacuum condition is required while nitrogen adsorption throughout the sample is recorded. Finally, μCT can be performed on samples under aqueous conditions but requires radiation exposure [9, 62, 63]. Consequently, these methods are not useful as quality control methods for large scale scaffold production or for long-term in-situ monitoring.

Electrical impedance spectroscopy (EIS) has been used to study the microstructural properties of a variety of porous materials ranging from cement to

ceramics while resulting in negligible damage to the sample [62, 63]. EIS allows for the study of the effects of various composites added to a central material as well as long term evaluation of material stability under different conditions [62, 63]. In addition to porous materials, EIS has also been used as an evaluation tool for tissues providing information regarding the status of the tissue over time [62, 64, 65] and tissue morphology [66].

EIS uses a two or four conductive probe set up in samples with conductive media. As alternating current passes between the probes through the sample, it travels the path of least resistance which is, in this case, the pores filled with conductive media. Because the source current is alternating, it can be sent over a specified frequency range. The resistance along the current path at each frequency is recorded as the complex impedance, which consists of both the real and imaginary components, as well as the phase shift which can be translated to porosity [62, 65]. Despite the introduction of small metal probes, EIS does not cause any immediate or long-term damage to the sample being tested as long as a relatively low current density is used. As a result of EIS's usefulness in studying porous structures, it was chosen as a method for the nondestructive evaluation of tissue engineering scaffolds.

The model scaffold material chosen for evaluation is chitosan. Chitosan is produced through the deacetylation of chitin which is the naturally occurring polysaccharide comprising the exoskeletons of crustaceans. The resulting chitosan contains charged end groups which allow it to dissolve readily in weak organic acids and forms a regular structure of a porous sponge-like matrix upon redessication. Chitosan has demonstrated a high level of biocompatibility when used as implant material and is resistant to bacteria [67]. The pore structure of chitosan scaffolds has been shown to be

larger in diameter than that of the average cells [32]. Additionally, the chitosan scaffolds exhibit high porosity and well interconnected pore structure. The biocompatibility and pore characteristics both suggest that chitosan is an appropriate material for cell scaffolds [32] and therefore an ideal model scaffold for these experiments.

Since the chitosan scaffold shows good potential as a tissue engineering scaffold, it now becomes necessary to nondestructively characterize and monitor the scaffold under *in vivo* conditions. In our studies, EIS was first used to characterize the pore geometry. The results were compared to the more common scaffold characterization methods of SEM and MIP in order to determine its viability as a nondestructive technique for evaluating porosity and pore interconnectivity. The overall goal of this comparison is to demonstrate that EIS is a comparable and effective method which can be used for both initial characterization and continued monitoring.

3.2 Materials and Methods

3.2.1 Scaffold Fabrication

Chitosan scaffolds were fabricated by dissolving 2% weight per volume dry chitosan powder from crab shells in 2% volume per volume acetic acid (all from Sigma, St. Louis, MO) heated to 50°C. The chitosan solution was cast into a specimen container to an approximate fill level of 3 cm high and frozen at -20°C for 24 hours. Once thoroughly frozen, the scaffold was lyophilized for 24 to 36 hours resulting in a foam-like 3D matrix. The sample was ensured to be completely dry by piercing the center of the scaffold with a 20 gauge needle in order to feel for irregularities indicative of insufficient freeze drying. A total of eight scaffolds were fabricated from separate batches in order to test the consistency of the results acquired from the EIS.

3.2.2 Characterization

Scanning Electron Microscopy (SEM)

In order to image the scaffold with SEM, a completely dry scaffold was removed from the lyophilizer and cut into wedges thereby exposing interior surfaces. The sample slices were kept with desiccant prior to sputter coating with gold. The sample was then imaged on a SEM (Amray 1830, Bedford, MA) using an accelerating current of 25 kV and recorded at resolutions of 60X to 200X. The obtained images were analyzed using the NIH Image J software. Each usable pore was outlined and the 2D area was determined by measuring at the same orientation across the visible pore diameters. Statistical analysis (average and standard deviation) was performed.

Mercury Intrusion Porosimetry (MIP)

Mercury intrusion determines pore geometry and pore volume by introducing mercury, which is a non wetting liquid, into the dry scaffold under pressurized conditions. Samples placed in a penetrometer are subjected to high vacuum. Once the minimal pressure is achieved inside the glass penetrometer, mercury flows, to surrounding the sample. This initial volume of mercury subtracted from the known volume of penetrometer provides the volume of the sample if it were completely solid. Pressure is then applied to the reservoir of mercury in the penetrometer stem at increasing incremental installments. With increased pressure, the mercury enters increasingly smaller pores. The total volume of mercury forced into the sample is used to determine the overall porosity while the mercury at each pressure interval allows for the estimation of pore size.

Three wedge portions were sliced from three separate chitosan scaffolds and analyzed with a mercury porosimeter (Micromeritics Autopore IV, Norcross, GA). First, a vacuum of 50 micrometers of mercury was pulled on each sample thereby completely removing the air from the sample. Mercury then surrounded the sample and was forced into the pores from large to small with increasing pressure from 0.22 psia up to 30 psia. The weight of the sample in the penetrometer was determined both prior to and following the introduction of mercury. The difference in weight divided by the density of mercury at room temperature gives the total volume used. By dividing the total pore volume by the external volume of the sample, porosity or percent pore volume was determined. The pore size was estimated using the Washburn equation:

$$r = 2s\cos(\Theta)/p, \qquad\qquad [3.1]$$

where r is the pore radius, s is the surface tension of mercury, Θ is the contact angle of the mercury and p is the pressure applied. A built-in algorithm automatically calculated this value at each pressure interval and averages them after all points were taken.

Electrical Impedance Spectroscopy (EIS)

The electrical impedance spectrometer (Figure 6) consists of an AC generator, the left and right sample electrodes and the impedance analyzer which also inputs the signal into the computer for data collection. The AC generator operates at a constant current while sweeping across a predetermined frequency range starting with the highest to the lowest. At each frequency, the impedance analyzer measures the complex impedance. Each data point consists of the impedance magnitude, real and imaginary impedance, and phase shift. EIS was initially performed on two dry scaffold samples using 6Al 4V ELI medical grade titanium wire probes (Small Parts, Inc, Miramar, FL) attached to an

impedance analyzer (Solartron, 1260A, Hampshire, England). The sides and bottom of

the scaffold were sealed with wax to prevent current leakage.
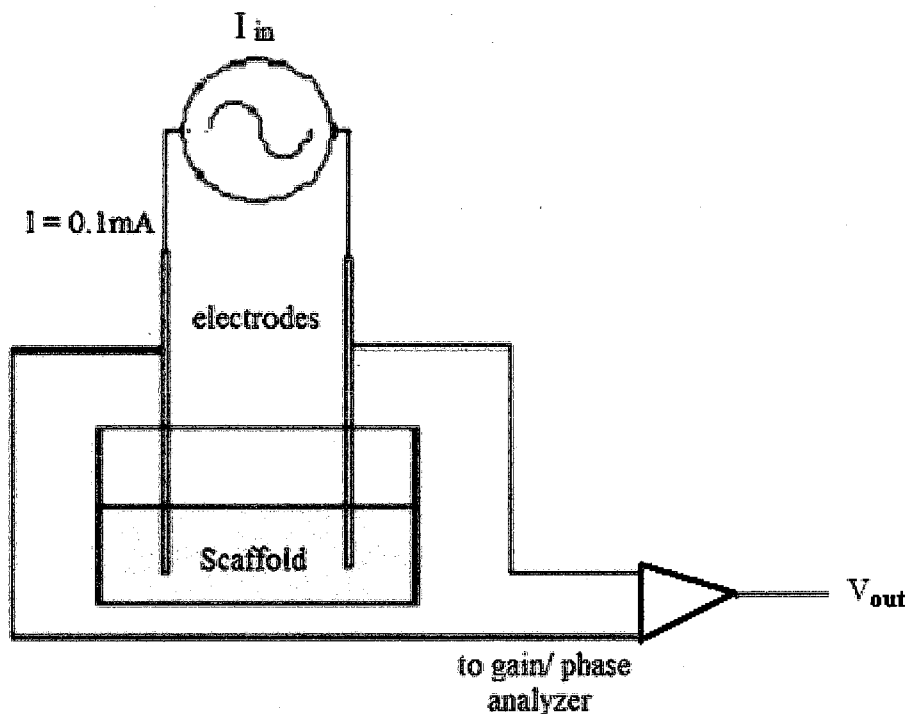
Figure 6: Electrochemical impedance spectroscopy setup showing parallel electrodes
introducing a constant current of 0.1mA into the chitosan scaffold.

A constant current of 0.1 mA was used for the evaluation and scanning was

performed over the frequency range of 10^{-2} to 10^4 Hz. The scaffolds were then swelled

with deionized water until reaching total saturation, followed by EIS using the same

current and frequency range. Subsequently, phosphate buffered saline (PBS) was

introduced into the scaffold at the increments of 20%, 29%, 50% and 100% with EIS

performed at each increment with identical parameters. The five remaining scaffolds

were each sealed with wax and swelled with non-diluted PBS. Each was evaluated with

EIS with a constant current of 0.1 mA over the frequency range of 10^{-2} to 10^4 Hz.

3.2.3 Data Analysis

The magnitude of impedance was plotted against the frequency. The impedance of the sample was observed over the frequency range and the effect of ionic composition on the shift of the impedance magnitude was examined. The tangent of this phase shift is the ratio of the imaginary permittivity (ε'') to the real permittivity (ε'):

$$\tan(\Phi) = \frac{\varepsilon''}{\varepsilon'}. \hspace{3cm} [3.2]$$

The imaginary permittivity is the loss permittivity relating to the resistive nature of the sample while the real permittivity is the storage permittivity relating to the capacitive nature. The tangent of the absolute value of phase shift was computed for the frequency range thereby providing the ratio of resistive to capacitive component.

By plotting the real versus imaginary impedance in a Nyquist plot, the bulk resistance was acquired. Using a form of Archie's law, porosity was estimated from the bulk resistance by first calculating the effective conductivity:

$$\sigma_{eff} = \frac{l}{R_b A}, \hspace{3cm} [3.3]$$

where σ_{eff} is the effective conductivity, R_b is the bulk resistivity, A is the cross sectional area and l is the sample length. Archie's law was used to determine the porosity by the following equation:

$$\sigma_{eff} = C\sigma_0 \Phi_0^m, \hspace{3cm} [3.4]$$

where σ_0 is the conductivity of saline which is known to be 1.2 S/m [68], Φ_0 is the pore volume or porosity, C is the coefficient of saturation ranging from 0.1 and 1, and M is

the cementation factor typically in the range of 1.5 to 4. Calculation details provided in Appendix B.

Once the sample porosity was calculated, the pore connectivity was determined. There is a connectivity factor (β_p) for the pores as well as the solid material which are related to the effective conductivity of the saturated scaffold as seen in the following equation [63]

$$\sigma_{eff} = \sigma_p \phi_p \beta_p + \sigma_s \phi_s \beta_s,$$ [3.5]

where σ_{eff} is the effective conductivity; σ, Φ, and β are the conductivity, volume fraction and connectivity factor with p and s referring to the pores and scaffolds respectively.

3.3 Results and Discussion

Scanning electron microscope (SEM) analysis showed a consistent pore structure throughout the scaffold (Figure 7) except the slicing location. As a result of the cutting that compromises the region, it was eliminated from the data analysis. Regions in which pores were deemed to be completely intact were analyzed. Under the assumption that the pores are sectioned past the mid point the opening remains circular but decreases consistently in size (Figure 7), the diameters were determined for each pore. The average diameter was determined to be approximately 107.31 ± 24.05 µm and the median value was 119.45 µm. Pore diameters ranged from as low as 60.8 microns and as high as 159.23 µm (Figure 7). Some aberrant larger pores were noted; however, these are likely the result of being on the uppermost surface during lyophilizing. Internal sections fall primarily within the aforementioned range.
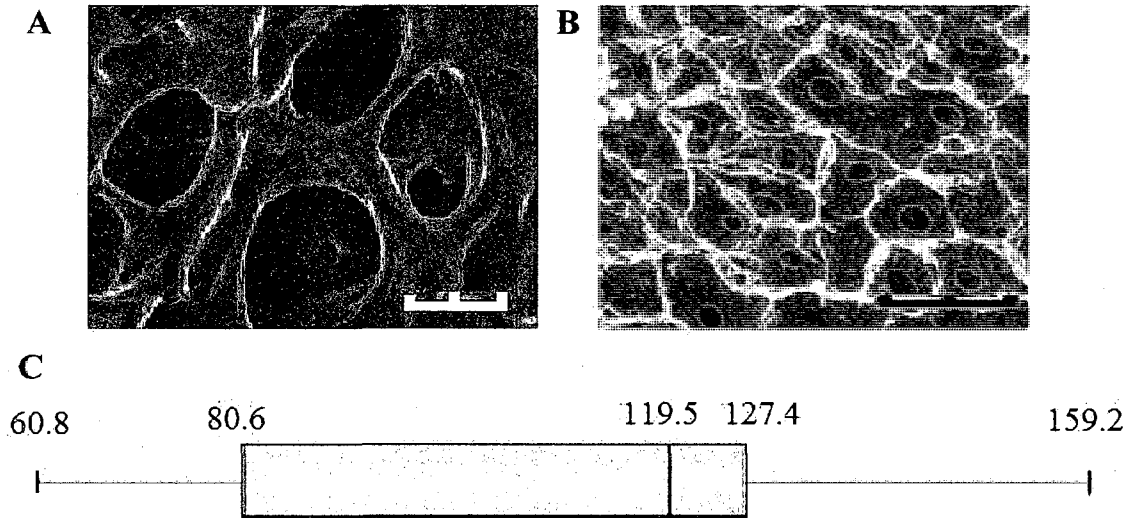
Figure 7: A) SEM scan of chitosan scaffold at 25KV showing pores with average diameter of 107.31 ± 24.05 μm. B) SEM scan of chitosan scaffold with 20 KV showing consistent decreasing circular cross section. C) Distribution of pore sizes determined from image analysis. Scale bar =100 μm (A) and 50 μm (B).

For the four samples tested with a mercury contact angle of 130° and a density of 15.534 g/ml, the average porosity was found to be 72.9 ± .49% using MIP. The average of the three samples gave a pore diameter average of 82.2 ± 4.79 μm. These values are consistent with results in previous studies [32].

A sample plot of cumulative intrusion volume versus pore size was generated for one of the three samples (Figure 8). The steep drop and plateauing of the plot indicates that the pore diameter range is very narrow for the scaffold thereby further corroborating the SEM images.
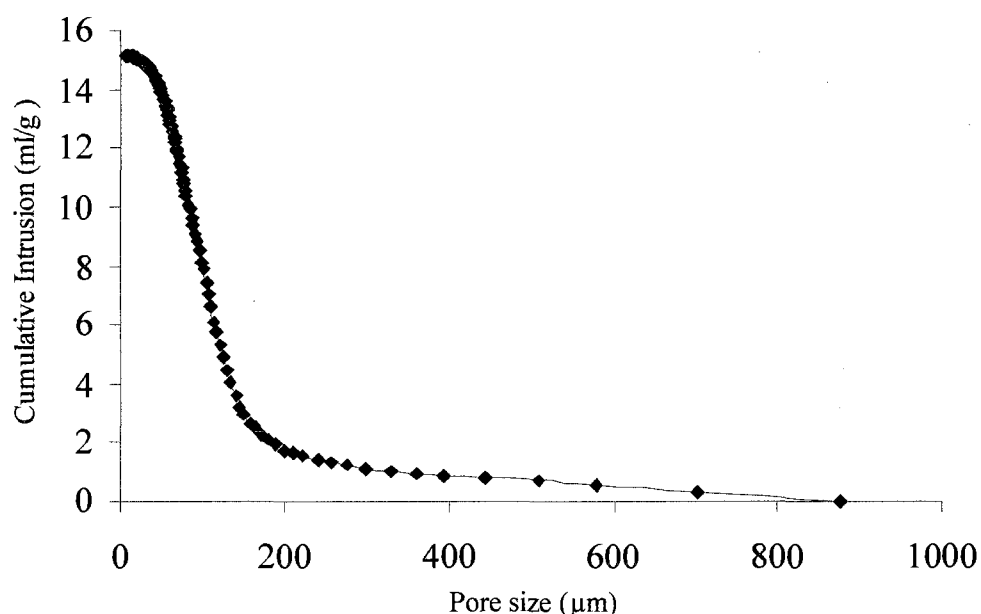
Figure 8: Plot of cumulative intrusion volume per pore size from mercury intrusion porosity analysis of a sample chitosan scaffold.

The first EIS test was run without the addition of any liquid and resulted in expected high impedance across the frequency (data not shown). The addition of DI water reduced the impedance values from the dry sample due to the presence of charged species from the dissociation of water molecules into hydronium and hydroxyl ions; however, the values were still high. With each increase in ionic strength, the overall impedance of the sample was reduced. The reduced impedance is a direct result of the increase in the number of ionic species in the solution. Altering the PBS concentration resulted in the shifts in impedance noted in five EIS data sets (Figure 9).
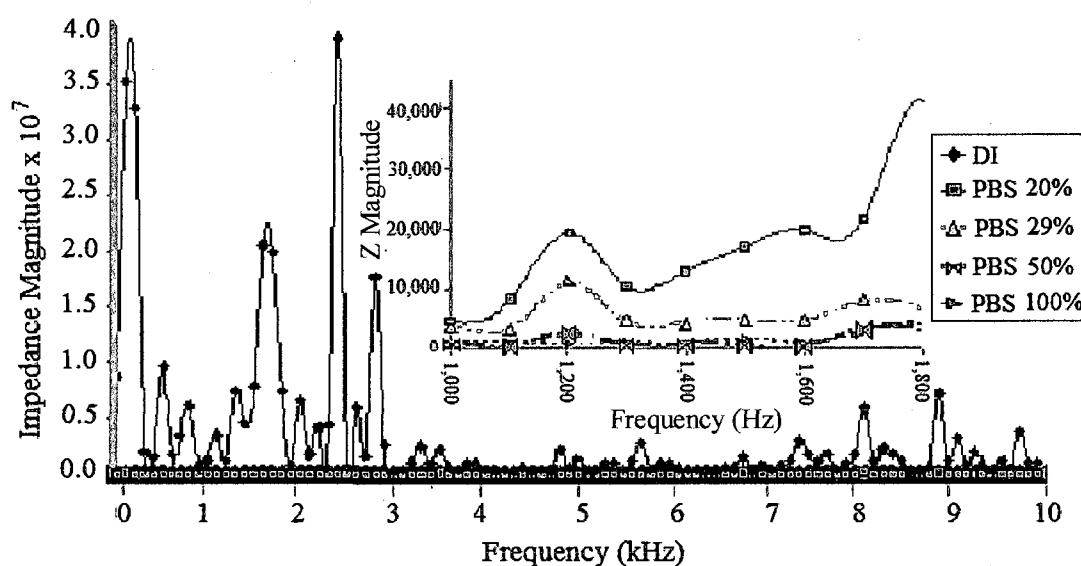
Figure 9: Impedance magnitude over the frequency range as determined by electrochemical impedance spectroscopy with titanium probes showing the decreasing magnitude with increasing ionic concentration. Inset: Close up view of frequency under 2 kHz (dry sample not shown).

The data for the samples containing 100% PBS and DI water were also compared over the same frequency range for the phase shift. The phase shift is the change in phase angle between the input and output waveform. The signal is altered by the material the current passes through resulting in a phase shift from the emitted signal to the resultant signal. While no correlation could be made to the frequency, the distribution of the permittivity ratio showed considerably higher values between 0 and 1 for the 100% PBS sample as compared to the DI water (Figure 10).
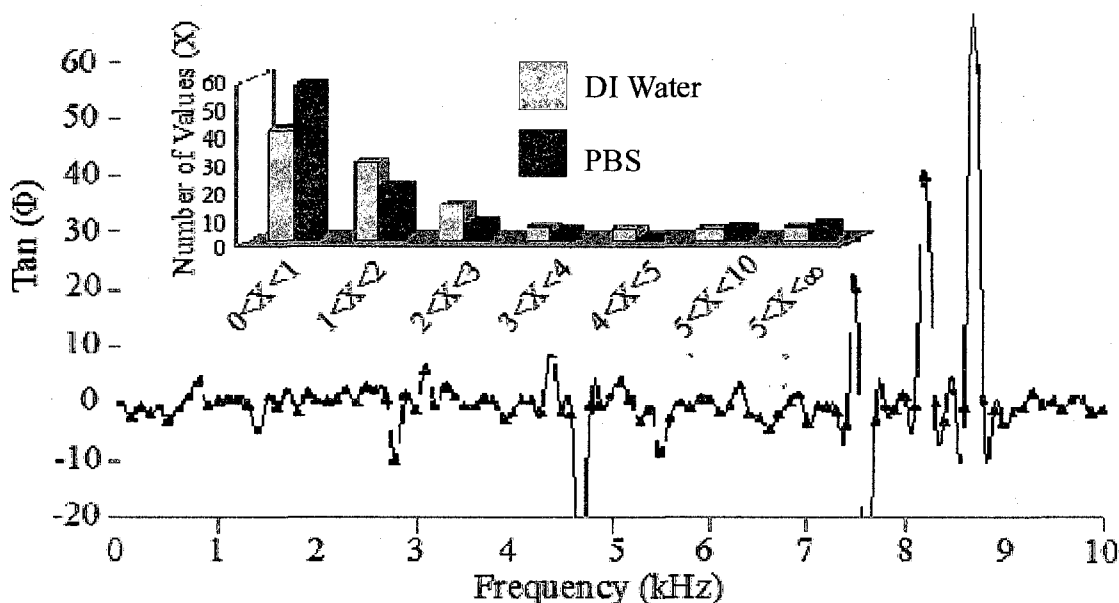
Figure 10: The phase shift expressed as tangent (representing the ratio of the imaginary and real permittivity) over a frequency range for the scaffold with deionized water. Inset: Distribution of ratio values for the tangent of the phase shift.

The values between 0 and 1 indicate that the resistivity of the sample is lower than the capacitance therefore the sample saturated with DI water is far more resistive than the PBS. Perhaps, the increase in ionic species in PBS lead it to act more like a capacitor where as DI water, due to the lack of ionic species, acts more like a non conductor. The next set of EIS data from five separate samples was collected and compared for consistency by two Bode plots. The Bode plots of the phase shift and the magnitude showed close grouping of the points indicating uniformity in both the sample and the testing method (Figure 11).
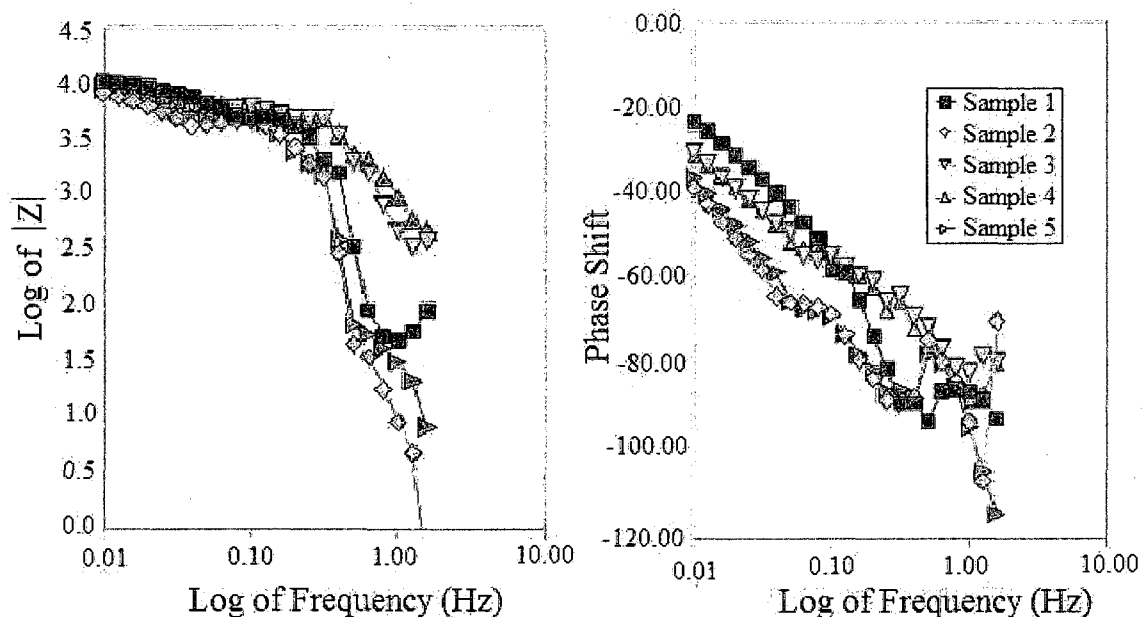
Figure 11: Bode plot of the impedance magnitude (left) and the phase shift (right) versus the frequency showing consistent behavior for all 5 samples.

Additionally, the two Bode plots took on the standard curvature for EIS for a single time constant system [69]. All samples were run under the conditions stated previously with the exception of sample 5. After the previous four had been run, it became apparent that the Nyquist plot required further scanning of the lower frequency range.

The Nyquist plots showing the real vs. imaginary impedance of the five sequential samples took on the characteristic semicircle shape for the lower frequency values (Figure 12). Given the normality of the shape, the bulk resistance (R_b) can be estimated as the point at which the semicircle crosses the X axis. Because only one of the samples was allowed to cross the X axis, the others were fitted to a semicircle in order to determine their approximate cross. In order to anticipate the X intercept of the Nyquist

plots, an approximate radius was estimated by taking the average of the real and imaginary impedance values at the visually observed center point, x = 5,300.
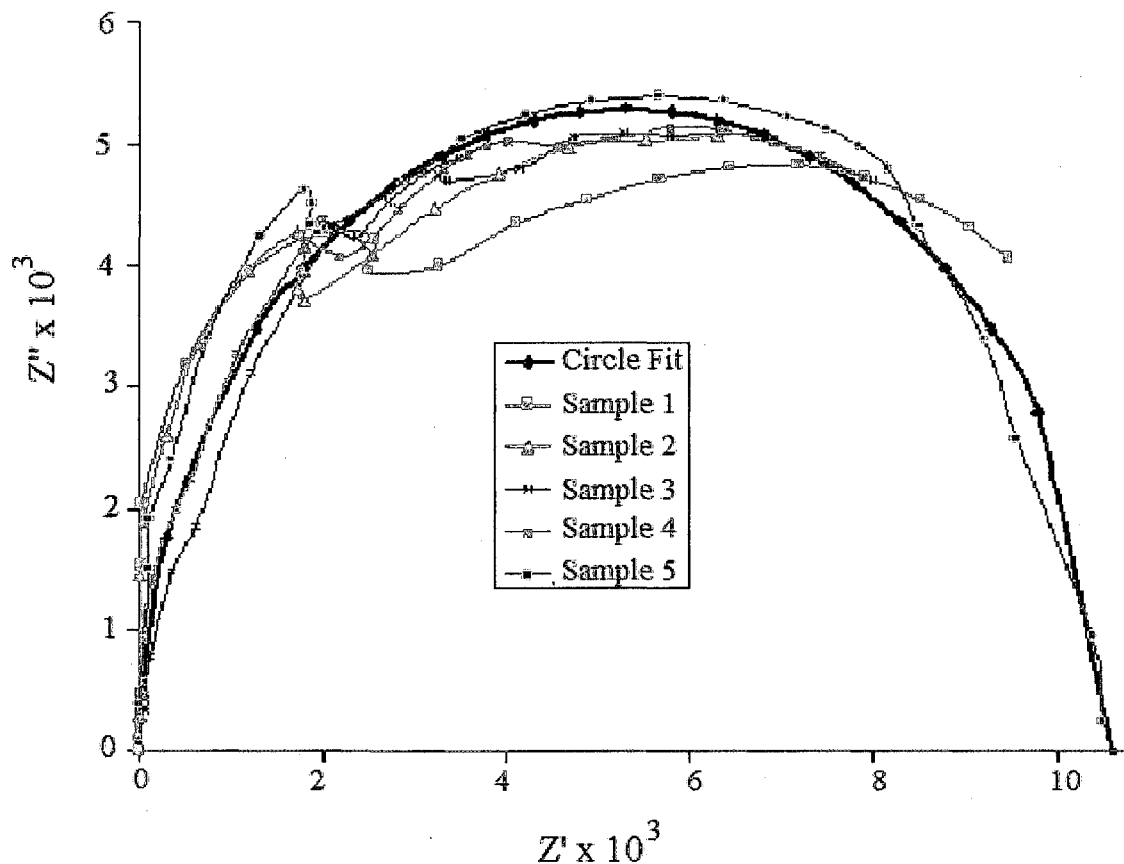
Figure 12: Nyquist plot of the real versus the imaginary impedance for 5 different chitosan scaffolds. Geometric projection of the semicircle (circle fit) indicates a bulk resistance value of 10,600 ohms.

Different samples gave slightly different values (Table 2). The average of the values totaled approximately 5,300. Using 5,300 as the radius, a semicircle was plotted (Figure 12) along with the impedance values showing a good fit which therefore suggests that the X intercept of the semicircle is approximately that of Nyquist plots: which is 10,600

ohms. As a result the new R_b was determined to be 10,600 ohms. A simple DC

resistance evaluation was performed confirming the EIS determined R_b (Data not shown).

Table 2: Estimated radii of Nyquist plots for chitosan scaffolds from approximate center
point of each arc (n=5).

Sample	Estimated Radius $\times 10^3$ ohms
1	5.20
2	5.28
3	5.19
4	5.29
5	5.53
Average	5.3 ± .14

While the formulas and interpretations of Archie's law have been widely

published for a number of different types of rocks [70], the use of EIS to characterize

tissue scaffolds is novel. Consequently, the behavior of the scaffold must be taken into

account in order to obtain the correct equation format. Because the scaffold becomes

completely engorged with PBS, it can be assumed that C is at or near 1 due to the total

saturation. The cementation factor is harder to estimate from physical observation. In

1999, the results of a fused glass bead experiment were reported showing a relationship

between porosity and the inverse of the formation factor (F) which is σ_{eff}/σ_0. The

experimental setup included the development and characterization of physical porosity

models composed of three different sized glass beads. The data collected showed that the

physical models fit the mathematical model proposed with the use of $C=1$ and $m=2$ [71].

This model also applies to physical systems with porosity in the anticipated range of the

chitosan scaffold so the values of $C=1$ and $m=2$ are taken from this point forward in the characterization.

Using the R_b determined from the Nyquist plot, the effective conductivity was determined to be 0.605 S/m. Introducing the effective conductivity into Archie's law, the porosity was estimated to be 71.0%. The pore connectivity factor can not be determined from either of the previously discussed methods; however, evaluating the connectivity is important in order to assess fluid flow. When the scaffold is saturated with an electrolytic solution the contribution of the pore to the effective conductivity far exceeds the contribution of the solid components of the scaffold. As a consequence, the solid portion of the equation 3.5 can be considered null and the equation can be rewritten in the following format in order to solve for the connectivity

$$\beta_p = \frac{\sigma_{eff}}{\sigma_p \phi_p}. \qquad [3.6]$$

The effective conductivity was once again used to determine the pore connectivity factor, which is 0.71, a reasonable number given the relationship between porosity and pore connectivity [63].

Based on physical observation of the scaffold prior to, during, and following the performance of EIS analysis, it became apparent that the physical damage from the testing was minimal. The purpose of the wax technique is solely to prevent current leakage. For use *in vivo*, this wax coating would not be necessary due to modification in the casting procedure. The ionic strength variation experiments resulted in the expected correlation of lowered resistance with increased ionic strength. The results of these findings include the assessment that the primary contributor to the EIS data is the fluid in the pores and that the testing can be optimally performed under subtly varying in *vivo*

conditions. The phase shift evaluation confirms once again the critical effect of the pore fluid as well as the overall slight capacitive nature of the scaffold when filled with PBS. Based on the testing parameters with PBS, the scaffold can be evaluated under *in vivo* conditions.

The SEM data for pore diameter agrees with previously published data [32] and corresponds to the value of pore diameter provided by the MIP (Table 3). By comparing the visual data with the physical intrusion data, we can further legitimize the results of the MIP providing confidence in the value of 72.9% for porosity. The calculated value for porosity of 71.0% from EIS is therefore not only close to the value acquired from the proven method but also legitimate. The additional value of 0.71 for the pore connectivity factor provides characterization that heretofore was unattainable by the commonly used methods. This pore connectivity factor indicates a high level of connectivity that can be associated with softer flow of nutrients and waste to and from regions of the scaffold.

Table 3: Pore size and porosity comparison for scanning electron microscopy, mercury intrusion porosimetry, and electrical impedance spectroscopy

Method	Pore Diameter (μm)	Porosity	Comments
SEM	107.31 ± 24.05	-	Not tested for porosity
MIP	82.22 ± 4.79	72.9 ± .49 %	Dry Sample in Vacuum
EIS	-	71.0%	Sample in Aqueous Conditions

3.4 <u>Conclusions</u>

In summary, the data acquired and interpreted from the EIS compares favorably to the more commonly used characterization methods MIP which was visually confirmed by SEM. This comparison indicates that the EIS provides an effective nondestructive way of characterizing the pore properties of the chitosan scaffold. Furthermore, EIS provides the opportunity to monitor the scaffold long-term under *in vivo* conditions.

CHAPTER 4

ELECTROKINETIC PARTICLE TREATMENT

4.1 Introduction

While chitosan has been shown to be an effective material for tissue engineered scaffolds [27], chemical and physical modifications to the scaffold environment may increase the efficacy of the composite. Additions such as hyaluronic acid, growth factors in the form of proteins, and even ceramic particles have been used to alter everything from cellular differentiation to the mechanical strength [72, 73]. Often these modifications are introduced during the initial production of the scaffold and many polymer scaffold materials will permit this. Chitosan; however, organizes itself into a regular pore structure by charged end groups on the chitosan molecule and exclusion during micro ice crystal formation.

The addition of particles during the fabrication stage of chitosan can disrupt the orientation of the charge groups and compromise not only the stability of the scaffold but also the shape and number of pores. It is this alteration in structure that prohibits this kind of modification to chitosan scaffolds during fabrication. Saturation of the chitosan scaffold in concentrated solution has resulted in modification without disrupting the structure [74] and small particles can be self incorporated if the scaffold is submerged

in a suspension of the desired modifier. In order to accomplish this, the particle size must be considerable smaller than the pores themselves and the pore connectivity must be high.

For tissue engineered scaffolds, it is not only desirable to alter the scaffold prior to the introduction of cells but also following their implantation. This need further requires that the modification be performed under conditions conducive to cell viability. In order to facilitate change without limiting functionality, electrokinetic treatment using a physiologically acceptable voltage range was implemented to effectively modify the chitosan scaffold. Three particles were chosen for this treatment protocol: hydroxyapatite nanoparticles, iron oxide microparticles, and hydroxyapatite microparticles.

The goal of this treatment was not to reduce porosity. Reduction of porosity minimizes the pore volume that could be occupied by cells. The purpose of the particle introduction is to demonstrate that the scaffold chemical properties can be modified by this process. While iron oxide and hydroxyapatite were chosen primarily as model particles to witness the effectiveness of each size, all of the particles have potential applications in the scaffold environment. Hydroxyapatite has been shown to increase adhesion and proliferation of osteoblasts [75]. Iron oxide has demonstrated potential for increasing membrane permeability [76]. In order to evaluate the effectiveness of the electrokinetic treatment, the porosity will be measured simply as a means of determining the level of particle intrusion, however; all treatment protocols will also be evaluated visually in the event that the volume of particles is too low to detect a notable drop in porosity.

The application of a potential difference to a porous structure has frequently been used for biological molecules as a means of size differentiation. Gel electrophoresis is traditionally used to separate proteins and segments of nucleic acids by inducing travel through a gel matrix with the application of an electromotive force. The orientation of the electrodes to the sample well is chosen based on the natural charge of the material to undergo size exclusion. Negatively charged particles are drawn toward positive electrodes and vice versa. The gel formulation is chosen based on the anticipated particle size and the degree of crosslinking is adjusted to optimization the porosity for the application. A standard buffer provides the charge carrier for the facilitation of current carrying. Due to the macromolecule size difference, they travel at different rates with the smallest moving most readily through the porous gel matrix [46, 47].

Similar to gel electrophoresis, particles suspended in a solution can be used to modify a substrate using the same electric field. This technique has been used to alter everything from the substrate color to the enhancement of corrosion resistance in construction materials [77, 78]. The substrate to be modified is used as the electrode of opposite charge to the particle to be plated on the surface. The particles travel through the suspension fluid at a rate based on the particle size, charge and the viscosity of the of the suspension media. Contrary to gel electrophoresis, the particles will not be embedded in a matrix but simply deposited. Depending on the nature and charge of the particle, the deposition may be strongly attached or easily removed.

A combination of the matrix mobility of electrophoresis and the modification abilities of electrodeposition results in the electrokinetic enhancement of porous substrates. For environmental applications, DC currents have been applied to

contaminated soil for electrokinetic remediation. The current causes the charged contaminants to travel by a means of both electrosmosis and electrophoresis. The remediation relies on the drawing out of particles; however, the reverse can be applied to incorporate particles into a porous substrate therefore reducing porosity, increasing mechanical strength or altering the internal environment [79]. The application of an electric field has been demonstrated to remove water from a hydrated porous system [80] and more recently an applied current has been shown to incorporate nanoparticles into hardened cement paste [77].

These afore mentioned applications primarily utilized the electro-osmotic effect causing water to flow between the electrodes. With heavier particles and larger pores, this electro-osmotic effect may not be enough to facilitate transport. The nature of the pore diameter and the high interconnectivity would reduce the necessary solid surface charge and result primarily in stationary sites inside the scaffold. The unlikeliness of a strong electroosmotic flow means that the effect has been deemed negligible in contrast to the electrophoretic forces on the particle and will not be considered in the treatment protocol.

4.2 Materials and Methods

4.2.1 Preliminary Experiments
Performed with Rachel Gade

Chitosan scaffolds were modified by adding an additional 0.5% wt/vol 15 μm iron oxide micro particles to the 2% chitosan scaffold by sonication after the entire allotment of chitosan had been dissolved at 50°C. The suspension of iron oxide in the chitosan solution was cast into a specimen container and frozen at -20°C for 24 hours. Once

thoroughly frozen, the scaffold was lyophilized for 24 hours. The resultant scaffold did not have the standard appearance of other 2% chitosan scaffolds. In addition to the grey color, the scaffold appeared to have a disordered fiber structure. The scaffold was sliced into wedges and analyzed by SEM (*Amray 1830, Bedford, MA*).

4.2.2 Scaffold Fabrication

Chitosan scaffolds were fabricated by dissolving 2% weight per volume dry chitosan powder from crab shells in 2% volume per volume acetic acid (all from Sigma, St. Louis, MO) heated to 50°C. The chitosan solution was cast into a 3 cm diameter specimen container to an approximate fill level of 3 cm high and frozen at -20°C for 24 hours. Once thoroughly frozen, the scaffold was lyophilized for 24 to 36 hours resulting in a foam-like 3D matrix with a slightly reduced radius. The sample was ensured to be completely dry by piercing the center of the scaffold with a 20 gauge needle in order to feel for irregularities indicative of insufficient freeze drying. A total of nine scaffolds were fabricated from separate batches in order to test the three particle sizes chosen for intrusion. Each individual scaffold was split at half height providing a sample portion for the electrical stimulation and a control to remain uninfluenced in the particle solution for the duration of the stimulation. Prior to use, all scaffolds were kept dry with desiccant.

4.2.3 Intrusion Solutions and Suspensions

First, a suspension was made by adding 2% wt/vol iron(III) oxide to PBS (both from Sigma Aldrich, St Louis, MO) and ultrasonic agitation. Characterization data provided by the manufacturer indicates the particle size is approximately 15 μm and it was understood that the particles exhibited a negative charge [81]. The particle size required frequent resuspension via aspiration during the electrokinetic intrusion. The

second suspension generated was a 2% (wt/vol) of hydroxyapatite microparticles (Berkeley Advanced Biomaterials, Berkeley, CA) once again in PBS using ultrasonic agitation. The manufacturer provided a size characterization range of 100- 300 μm and an implicit weak positive charge [82, 83]. The final particle suspension in PBS was made with 200 nm nanoparticle hydroxyapatite (Sigma Aldrich, St Louis, MO) to a concentration of 0.5% (wt/vol) once again with an understood positive particle charge [82, 83].

4.2.4 Electrokinetic Treatment

Plexiglass cubes were constructed and sealed to waterproof tightness on five sides. The lid portion of the cube was drilled at four locations: two for the electrodes located one electrode radius apart and two to vent any byproducts of electrolysis. A pair of radial electrodes was fabricated from medical grade titanium (Small Parts, Inc, Miramar, FL). The outer electrode was a ring with a diameter slightly greater than the scaffold while the inner electrode was straight (Figure 13). Electric field lines can be estimated based on the equality of the charges when connected to a DC voltage source (Figure 14).
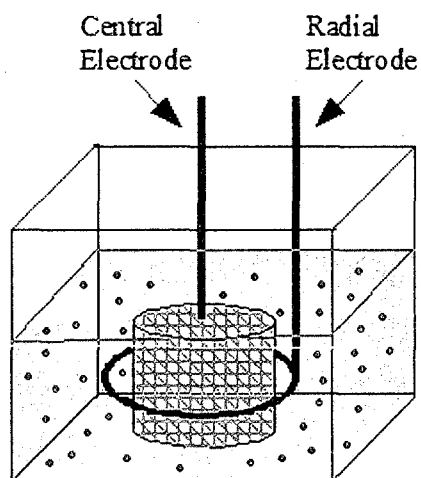
Figure 13: Electrokinetic particle treatment chamber with reversible radial electrode potential.
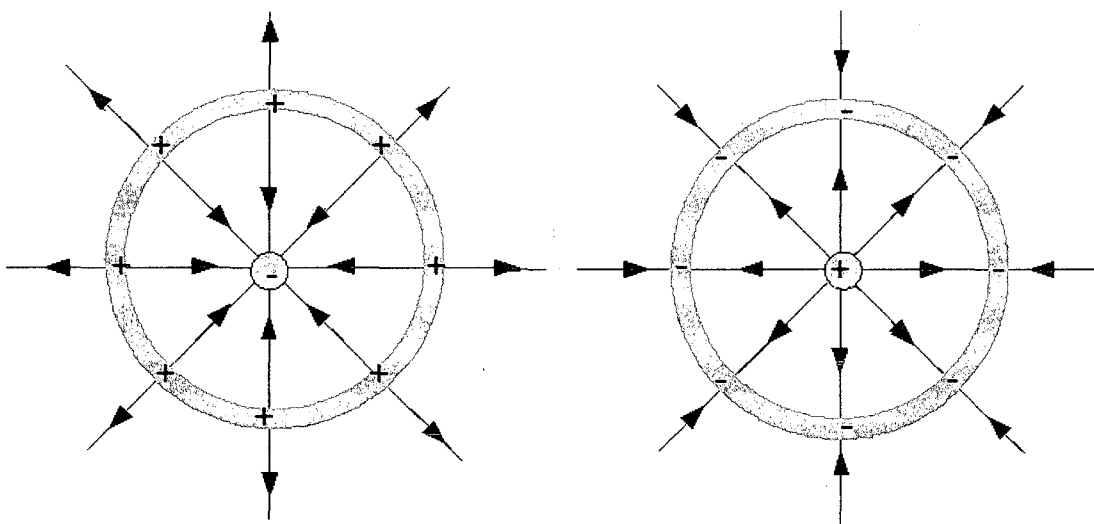
Figure 14: Electrical field lines for the hydroxyapatite (left) and iron oxide (right) electrokinetic set-ups.

The laterally sliced scaffold halves were coated on bottom with paraffin wax and attached to the bottoms of two electrokinetic set-ups. The paraffin assures that current will not leak under the scaffold and must flow through the scaffold. The center electrodes were inserted into the scaffolds and the outer circular electrode was placed

around the circumference of the scaffolds. The design of the outer electrode insures that it remains in close proximity to but not touching the outer walls of the scaffold. To prevent total dissolution of the scaffold, PBS was added in ml increments over several minutes directly to the scaffold. This also insures that the scaffold is pre wetted and that the particles could not be drawn in by the initial hydrophilic draw of the scaffold.

Once the scaffold was saturated, the particle suspension was added to each set-up and filled to level with the top of the scaffolds. Immediately following the introduction of the particle suspension, one of the two set-ups was attached to the DC power source at 4 V. This voltage was chosen based on previous cellular electrokinetics experiments which reported no effect on differentiated cells [50]. For the iron oxide suspension, the central electrode was the positive electrode and the outer ring was negative based on published data which indicates that in a solution of pH 7 such as PBS iron oxide particles exhibit a negative potential [81]. For both hydroxyapatite suspensions, the central electrode was negative with a positive outer electrode due to hydroxyapatite weak positive potential when unaltered and at neutral pH [82, 83]. Both the set-ups were maintained at the same ambient temperature and aspirated as needed to maintain the suspension.

Due to the application of current to water, the possibility of electrolysis always exists. While current used for the electrokinetic set up is very low, water will under go a redox reaction

$$4H^+ + 4e^- \rightarrow 2H_2 \qquad [4.1]$$

$$2O^{-2} \rightarrow 4e^- + O_2. \qquad [4.2]$$

The pH changes associated with the electrolysis might be of concern in the electrokinetic particle treatment; however, the buffer elements of PBS should negate any potential effects.

The duration of the electrokinetic intrusion and control was dependent on particle size (Figure 15) and charge. The electrophoretic velocity through the scaffold was roughly estimated by using a modified version of the of the equation for electrophoretic velocity (v) in a suspension for electrodeposition

$$v = \frac{QE}{4\pi r \eta},$$
[4.3]

where Q and r represent the approximate particle charge and radius. E is the voltage applied and η is the suspension viscosity [84, 85].
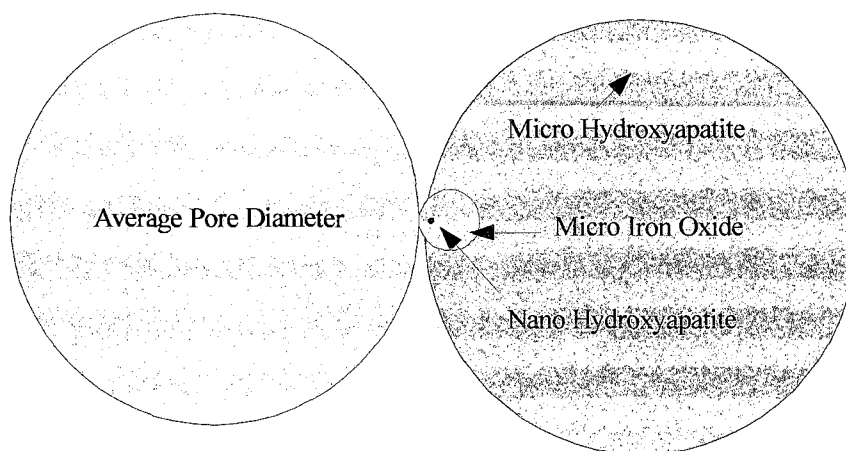
Figure 15: Diameter comparison of particles for electrophoretic transport against the average pore diameter ~100 μm.

In order to consider this equation for electrokinetic intrusion velocity, it must first be assumed that the distance between the outer electrode and scaffold is minimal as compared to the space between the outer electrode and the inner electrode so the primary

material that the particle will be traveling through is PBS swelled chitosan scaffold. Since information regarding engorged chitosan viscosity is not readily available, the projected viscosity for a 2% (wt/vol) agarose gel of approximately 10kPa·s will be used which is considerably more viscous than water but less viscous than a solid structure [86]. The 2% (wt/vol) agarose is an appropriate model because of its physiological buffer component and its reported pore diameter of ~100 μm [87]. Previous characterization of chitosan scaffolds has provided a pore diameter of approximately 100 μm as well. Particle charge was estimated by the charge per gram of each substance and the approximate number of particles per gram. All values for electrokinetic run time were rounded and based on travel from the outer edge of the scaffold to the center electrode (Table 4).

Table 4: Approximate treatment time determined by electrodeposistion rate (Equation 4.3) based on particle size and media viscosity.

Particle	diameter	approximate run time
Hydroxyapatite	200 nm	0.66 hours
Iron Oxide	15μm	6 hours
Hydroxyapatite	100-200 μm	43 hours

4.2.5 Characterization

Optical Evaluation

All scaffolds were sliced latitudinally prior to all subsequent characterization and observed under 10 X and 40 X magnifications with an upright microscope and the particle presence was qualitatively assessed.

Scanning Electron Microscopy (SEM)

The iron oxide electrokinetically treated scaffold was evaluated using SEM. This scaffold was chosen as a representative due to its median particle size in order to observe the pore incorporation of particle. In order to image the scaffold with SEM, it was frozen immediately following particle intrusion and lyophilized as if the scaffold were newly made. Once completely dry, the scaffold was removed from the lyophilizer and cut into wedges thereby exposing interior surfaces. The sample slices were kept with desiccant prior to sputter coating with gold. The sample was then imaged on a SEM (Amray 1830, Bedford, MA) using an accelerating current of 25 kV. The obtained images were qualitatively observed in order to note presence of particles in the pores. SEM (Hitachi S4800, Berkshire, UK) and energy dispersive spectrometer (EDS) were performed on both the electrokinetically treated and passive nano hydroxyapatite samples.

Mercury Intrusion Porosimetry (MIP)

Representative wedge portions were sliced from 3 electrokinetically treated chitosan scaffolds as well as 3 control scaffolds. Each scaffold had been desiccated as previously discussed for SEM and maintained desiccated prior to analysis with a mercury porosimeter (Micromeritics Autopore IV, Norcross, GA). First, a vacuum of 50 micrometers of mercury was pulled on each sample thereby completely removing the air

from the sample. Mercury then surrounded the sample and was forced into the pores from large to small with increasing pressure from 0.22 psia up to 30 psia. The weight of the sample in the penetrometer was determined both prior to and following the introduction of mercury. The difference in weight divided by the density of mercury at room temperature gives the total volume used. By dividing the total pore volume by the external volume of the sample, porosity or percent pore volume was determined. The pore size was estimated using the Washburn equation:

$$r = 2s\cos(\Theta)/p,$$ [18]

where r is the pore radius, s is the surface tension of mercury, Θ is the contact angle of the mercury and p is the pressure applied. A built-in algorithm automatically calculated this value at each pressure interval and averaged them after all points were taken. Previously acquired base line values for pore size and porosity of chitosan scaffolds were used for comparative purposes.

Electrical Impedance Spectroscopy (EIS)

Significant portions of the 3 treated/ control pairs were frozen and lyophilized as before and coated in paraffin wax on the sides and bottom when necessary to prevent current leakage. All scaffolds were swelled with PBS in order to fill the pores with an electrically conductive medium. EIS was performed on the scaffold samples using 6Al 4V ELI medical grade titanium straight wire probes (Small Parts, Inc, Miramar, FL) attached to an impedance analyzer (Solartron, 1260A, Hampshire, England). A constant current of 0.1 mA was used for the evaluation and scanning was performed over the frequency range of 10^{-4} to 10^{3} Hz. This approach has previously been used to

characterize chitosan scaffolds and has been shown to be effective and non destructive.

Appendix A provides elaboration and details for the chitosan fabrication, MIP, and EIS.

4.2.6 Data Analysis

By plotting the real versus imaginary impedance values acquired for all samples

in a Nyquist plot, the bulk resistance was determined. Using a form of Archie's law,

porosity was estimated from the bulk resistance by first calculating the effective

conductivity:

$$\sigma_{eff} = \frac{l}{R_b A},$$

[4.4]

where σ_{eff} is the effective conductivity, R_b is the bulk resistivity, A is the cross sectional

area and l is the sample length. Archie's law was used to determine the porosity by the

following equation:

$$\sigma_{eff} = C\sigma_0 \Phi_0^m,$$

[4.5]

where σ_0 is the conductivity of saline which is known to be 1.2 S/m [68], Φ_0 is the pore

volume or porosity, C is the coefficient of saturation ranging from 0.1 and 1, and M is

the cementation factor typically in the range of 1.5 to 4. Porosity values acquired were

compared to the previously acquired values for chitosan scaffolds. Appendix B shows

the details for the porosity calculations.

4.3 Results and Discussion

Preliminary experiments with suspended iron oxide microparticle scaffolds were

not as physically strong as standard 2% chitosan scaffolds and, upon slicing for SEM,

partially degraded. The intact regions were imaged with SEM showing an irregular pore

structure uncharacteristic of chitosan scaffolds (Figure 16). These results confirm that

the chitosan structure is compromised with the addition of microparticles.
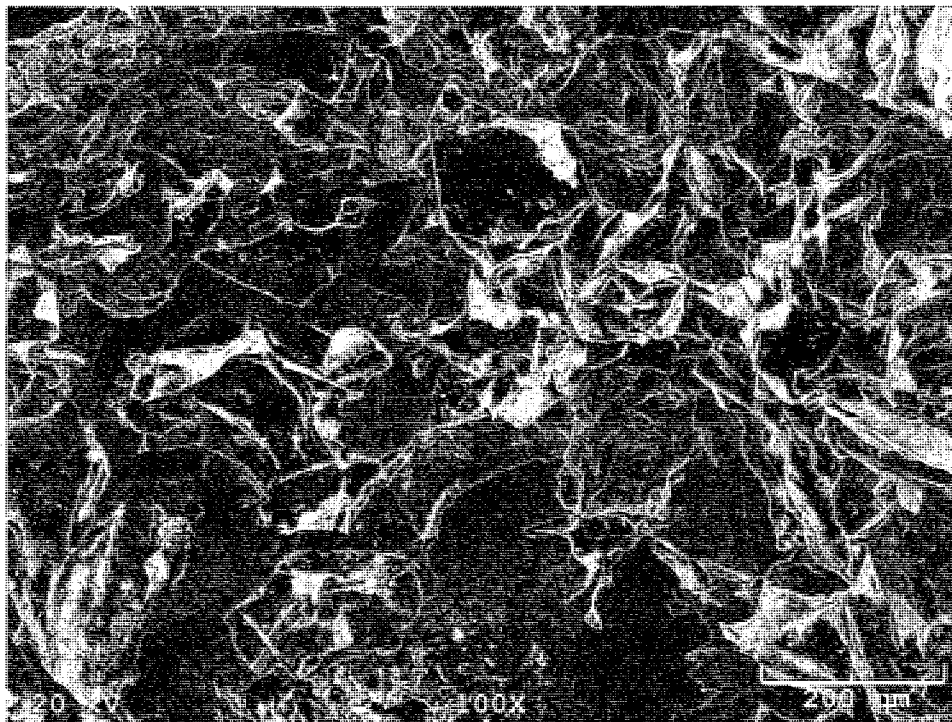
Figure 16: Scanning electron microscope image showing compromised pore structure
created with iron oxide modification during the scaffold fabrication process.

Microscopic observation of the treated and control sample indicated the presence

of both iron oxide and the nano hydroxyapatite particles. The nano hydroxyapatite was

only visible as clumps of powder at optical magnification. The latitudinal slice for the

iron oxide treated sample indicated a good distribution throughout the cross sectional area

while the control had very little particle concentration in the central area but still

noticeable presence in the outermost regions of the scaffold. The nano hydroxyapatite

particles were difficult to characterize based on their size and lack of contrast with the

scaffold itself; however, it was apparent that the particles were present in both the treated

and untreated scaffolds. The micro hydroxyapatite was visible but impossible to quantify based on the lack of contrast with the scaffold. Lack of particles inside both the treated and untreated was obvious. Few particles were present on the outsides of both scaffolds.

SEM scans of the electrokinetically modified iron oxide scaffold showed that the standard 100 μm pore structure was not altered by the particle intrusion (Figure 17).
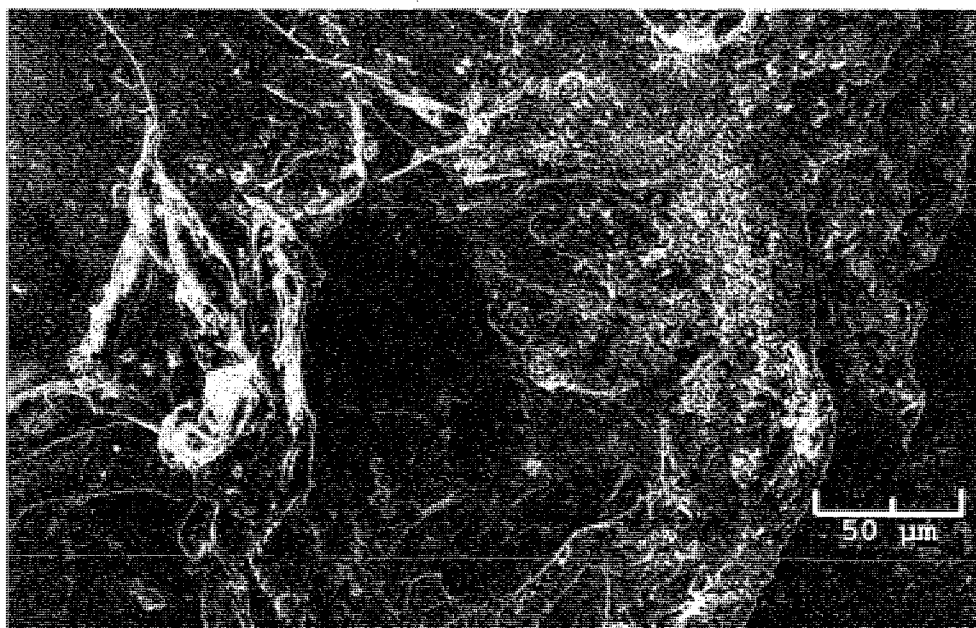
Figure 17: Scanning electron microscope image of iron oxide treated scaffold showing particles in relation to the pore.

Images of the center portions confirmed the optical microscopy findings that particles were present in the interior. Following the second desiccation of the scaffold for SEM scanning, particles appear to have localized themselves along the solid regions of the scaffold and appear to be somewhat attached. The iron oxide particles appear to clump around the pore openings while remaining relatively evenly distributed elsewhere.

This effect might be a result of the particles in the fluid volume of the pores that under go localized agglomerations during the desiccation.

SEM analysis of two nano hydroxyapatite modified scaffolds showed both a normal pore structure for the chitosan scaffold and large deposits of nanoparticles (Figure 18). The nanoparticles are not visible at the magnification which permits pore viewing. Consequently, magnifications of the regions have been provided next to the corresponding pore images. EDS (Figure 19 and Figure 20) confirmed that the nanoparticles contained calcium and phosphorous which are not present natively in the scaffold but are found in large proportions in the hydroxyapatite.
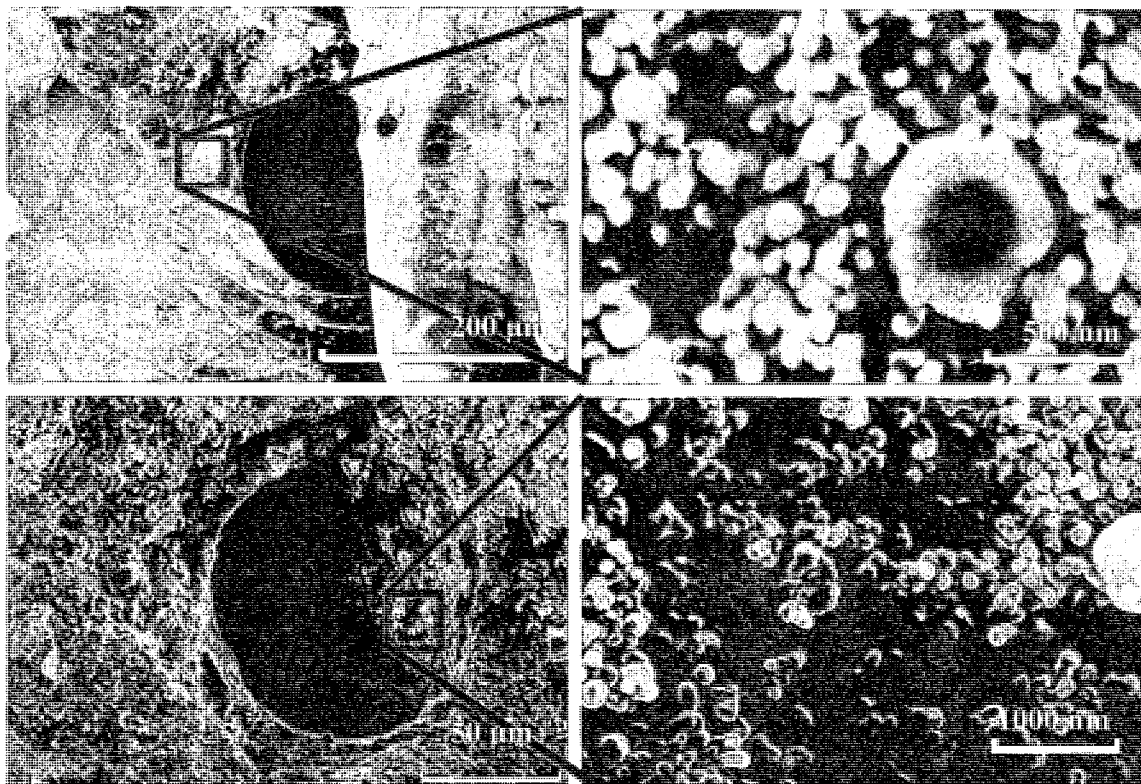
Figure 18: Scanning electron microscope images of the nano hydroxyapatite electrokinetically treated chitosan scaffolds showing normal pore structure (top left) and nanopatrticles (top right). The pore structure of the nonelectrokinetically treated scaffold was consistent (bottom left) and nanoparticles were also present (bottom right).
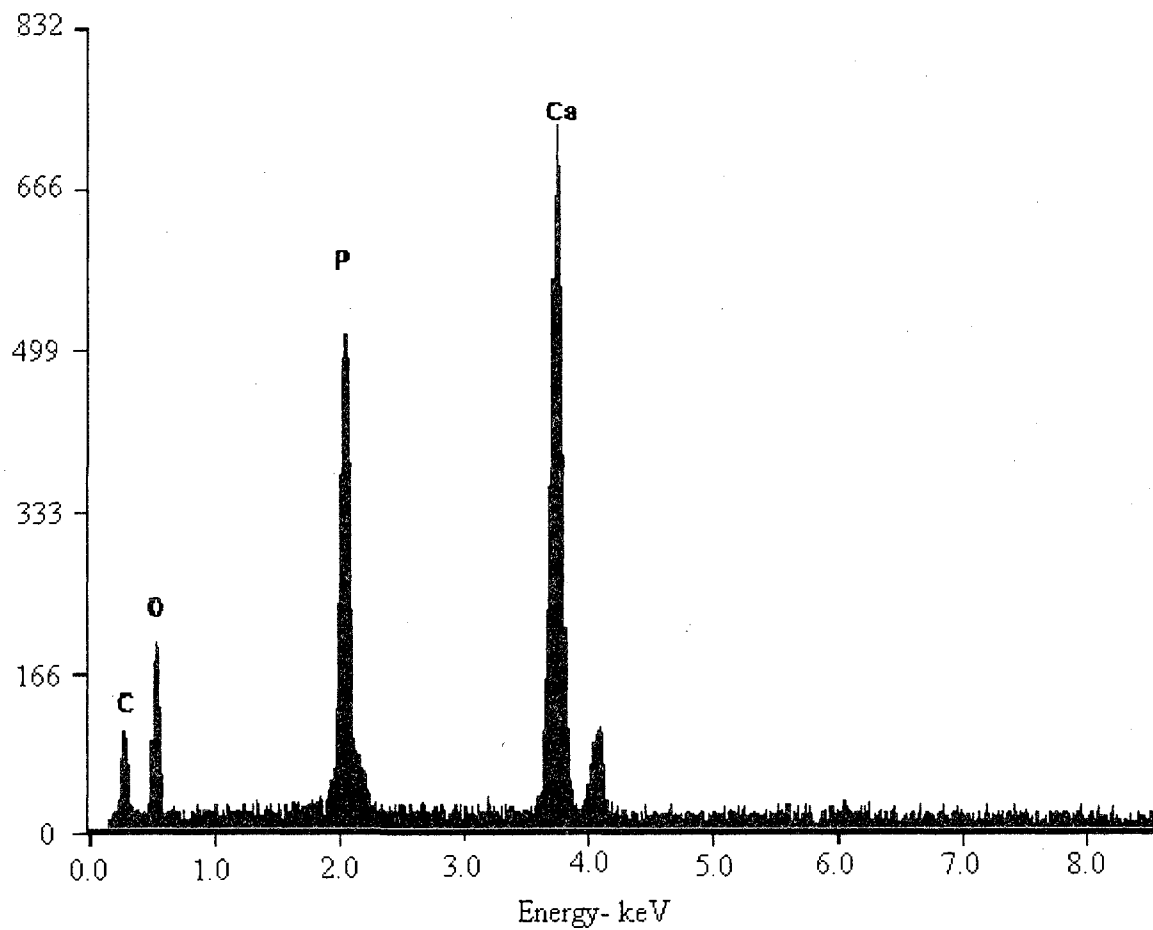
Figure 19: Energy dispersive spectrometer results showing peaks indicating the presence of calcium and phosphorous therefore confirming that the nanoparticles are hydroxyapatite in the electrokinetically treated scaffold.
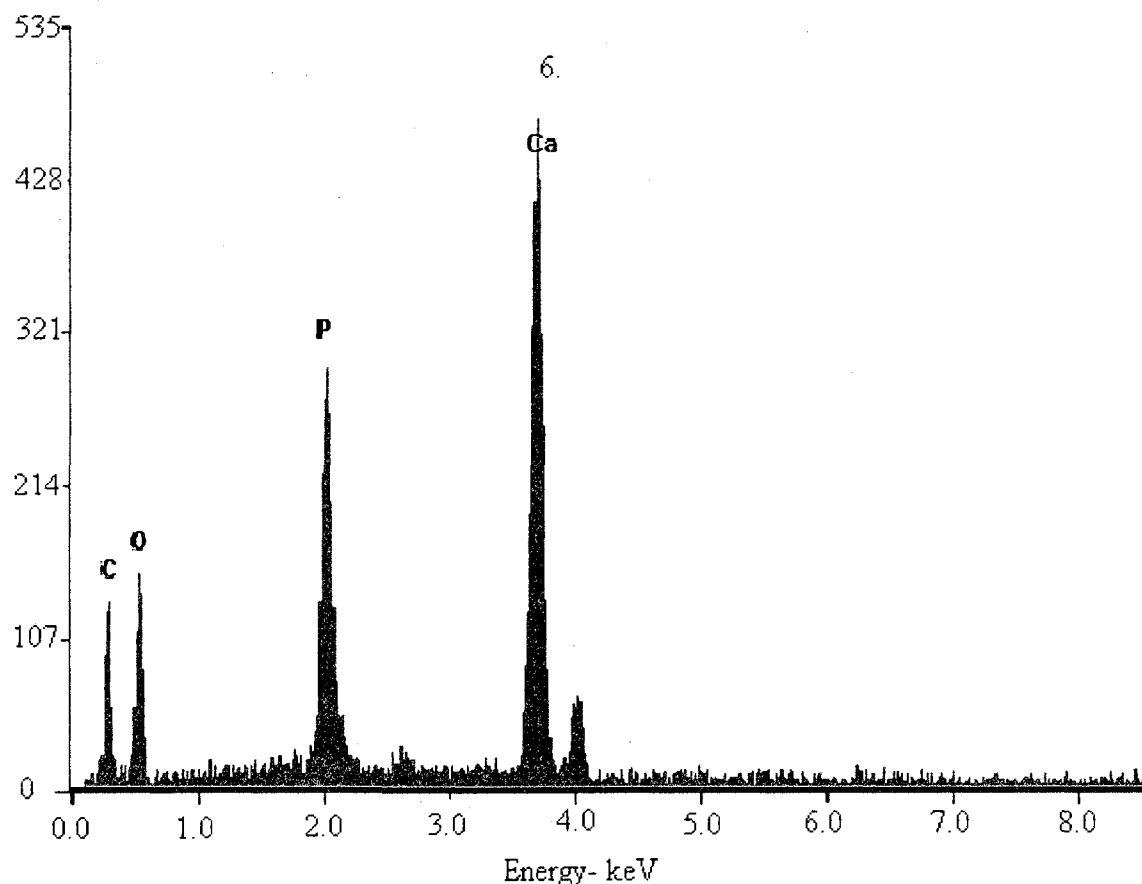
Figure 20: Electron dispersion spectra for particles present in the control nanoparticle
sample indicating that they are in fact hydroxyapatite due to the presence of
calcium and phosphorous.

MIP analysis of the treated and control iron oxide samples indicated a decrease in

porosity from a completely unmodified chitosan scaffolds with a slightly more significant

drop for the electrokinetically treated scaffold (Table 5). These drops in porosity

correspond to the notable presence of iron oxide microparticles which contribute to the

solid scaffold volume.

Table 5: Mercury intrusion porosimetry porosity values for the treated and untreated scaffolds.

Particle Modification	Particle Size	Porosity
Iron Oxide	~15 μm	71.98 ± .36%
Hydroxyapatite	~0.2 μm	72.88 ± .13%
Hydroxyapatite	~200 μm	73.01 ± .24%
None	-	72.9 ± .49%

Since the degree of attachment of the particles is unknown, the pore diameters reported from MIP may be compromised due to the possible dislodging of particles and accumulation in the pores during the pressurized intrusion. Regardless of whether or not the particles would be moved or extruded during the MIP procedure, the solid volume will remain constant in the results and is therefore legitimate. The standard MIP intrusion volume curve further indicates a smooth intrusion typical of successful testing (Figure 21).
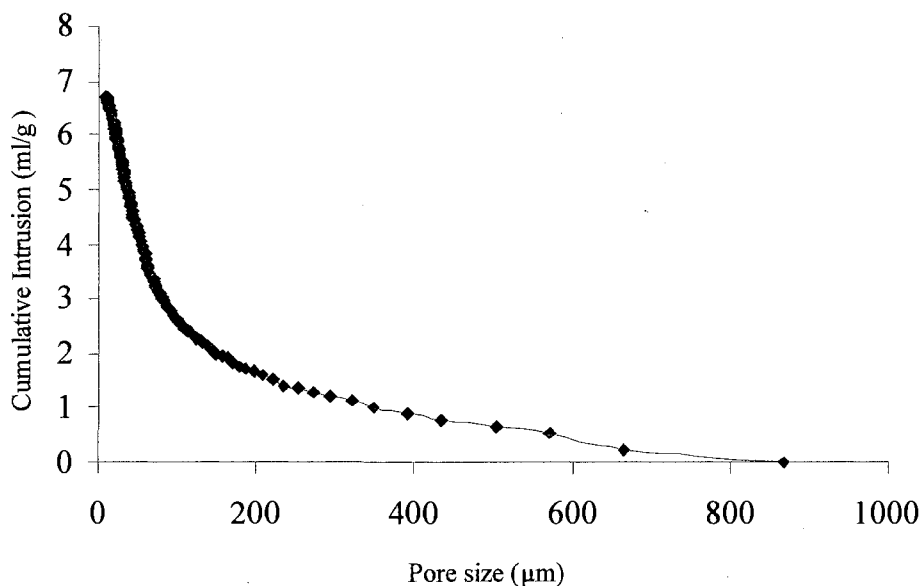
Figure 21: Cummulative intrusion curve for mercury porosimetry of iron oxide electrokinetically treated chitosan scaffold.

Analysis of variance (Table 6) performed on the iron oxide and control samples showed a significant difference between the porosity of modified and unmodified scaffolds.

Table 6: Analysis of variance for iron oxide and control scaffolds.

ANOVA

Source	DF	SS	MS	F
Factor	1	1.56	1.56	7.88
Error	5	0.99	0.198	
Total	6	2.55		

MIP analysis of the nano hydroxyapatite indicated a very subtle increase in porosity for both the electrokinetically treated scaffold and the control scaffold as compared to previously obtained data for unmodified scaffolds. The porosity values for

the treated and control scaffolds were insignificantly different (Table 5) (ANOVA not shown). The intrusion of nano hydroxyapatite particles with and without applied voltage is likely due to the size of the particles and their ease of movement through pores which are on average 200 times greater in diameter. The low charge present on the particle itself also contributes to the amount of electrokinetic treatment. Modification of the nano hydroxyapatite's surface area to increase the magnitude of charge might increase the volume of particles introduced due to increased electrophoretic activity.

The final scaffold treated with micro hydroxyapatite particles was analyzed with MIP and resulted in data indicating the pore size and porosity was not decreased from the unmodified chitosan scaffold. This lack of change corresponds to the microscopic observations indicating a lack of particles introduced into the scaffold. Previously reported and confirmed values for the average pore diameter of chitosan scaffolds agree that the pores are approximately ~100 μm across which is smaller than average micro hydroxyapatite particle diameter. The control sample demonstrated the hypothesized result that the micro particles would not flow into a pre-swelled scaffold. It is possible that the electrokinetic treatment may have been more successful if the charge on the hydroxyapatite had been modified and increased; however, it is unlikely that particles in the 100μm or greater diameter range would be usable at low voltage levels due to the prohibitively long treatment time and pore size.

EIS analysis of all of the samples both modified and provided the standard Nyquist plot curves but the changes in porosity were so small for the hydroxyapatite scaffolds that it was not possible to successfully distinguish them from curves generated from unmodified scaffolds (Figure 22). The iron oxide Nyquist plot showed an increase

in bulk resistance (Figure 23) which was applied to Archie's law in order to obtain a porosity of 70.2% which is a decrease from the previously determined unmodified value of 71.0% with EIS evaluation. This decrease in porosity corresponds to the decrease seen with MIP and corroborates the presence of iron oxide particles inside of the scaffold.
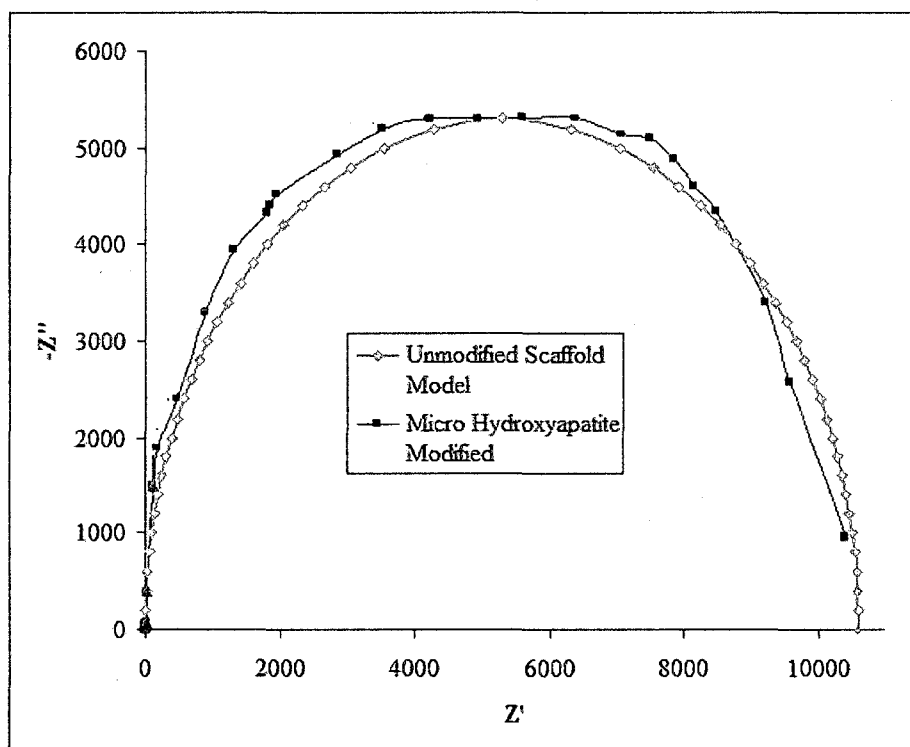
Figure 22: Nyquist plot of hydroxyapatite microparticle treated scaffold compared to the semi circular model for unmodified scaffolds.

If a double curve had been apparent in the Nyquist plot, it would have been indicative of a second resistive effect. The standard curvature of the plots did indicate that the charges of the particles did not really affect or react to the current used for EIS. Long term exposure to the EIS might have an electrokinetic effect on the particles but normal protocols do not. With the low current of 0.1 mA and a maximum duration of 1 hour the electrokinetic effect is minimal. If a higher concentration of the particles or

increased particle charge were used, the conductivity of the PBS would need to be modified when using EIS and Archie's Law as an evaluation technique.
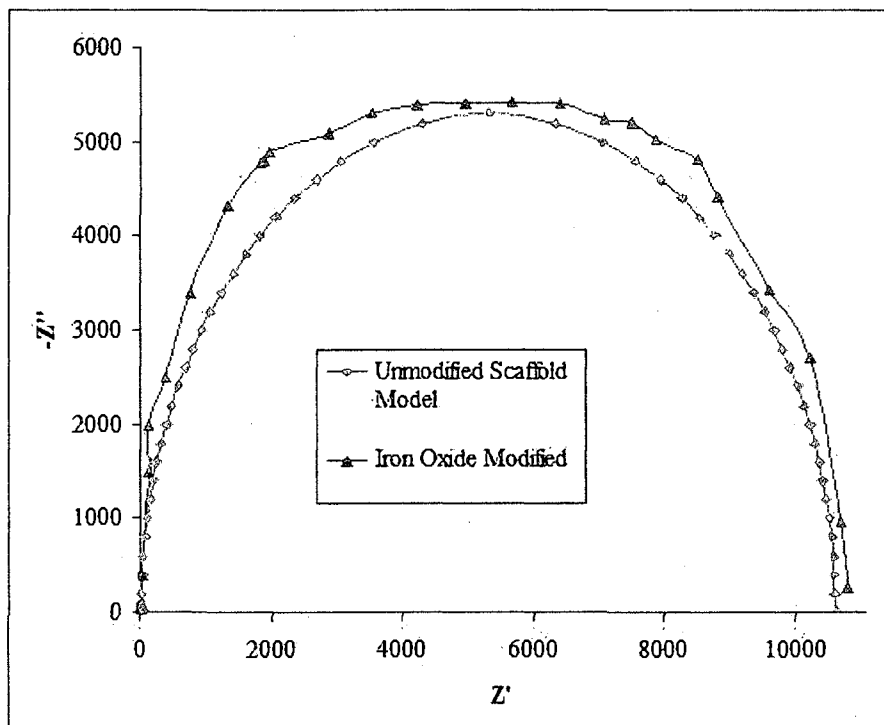
Figure 23: Nyquist plot of iron oxide microparticle treated scaffold compared to the semi circular model for unmodified scaffolds.

4.4 Conclusions

Optical and porosity evaluation techniques have shown electrokinetic intrusion to be successful for the modification of chitosan scaffolds when the particles are in the 15 μm arena as compared to simple exposure to the particle suspension without the potential difference. Larger particles in the same diameter range as the pores were realistically unable to be electrophoretically transported into the scaffold while particles in the nanometer range flowed freely both with and without the potential difference. The results of the particle diameter range under physiologically tolerable conditions have

shown potential for the electrokinetic treatment as a modification method both for acellular and cellular scaffolds when using particles in the 10 to 20 μm range.

CHAPTER 5

EVALUATION OF SEEDED CHITOSAN
SCAFFOLDS WITH EIS

5.1 Introduction

Bioimpedance has been successfully used as a characterization technique for tissues. The dielectric effect produced by the cell membranes as well as the polarization of proteins at limited frequency allows for comparison between tissues through plot comparison or model circuits. Biological impedance response to AC stimuli fits into three distinct regions (Figure 24) [54].
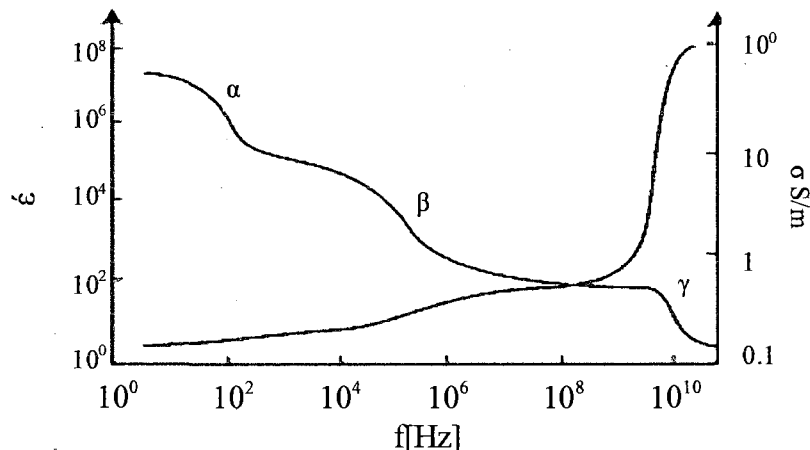
Figure 24: α, β, γ dispersion for impedance spectroscopy of tissue Chart from [54]

In the α dispersion, the primary effect of current stimulation in tissue is the diffusion of ions in the extracellular environment. If cellular gap junctions are open,

current can pass into and out of the cell as well but this effect will be minimal. In the β

dispersion, the cell membrane can be bypassed and a capacitive effect will take place. In

the upper β lower γ frequencies, proteins are polarized which can provide additional data

points if the protein concentration is great (Figure 25) [54].

    ⚘ = Cell with dielectric response
    ○ = Cell
    ⬡ = Scaffold Pore
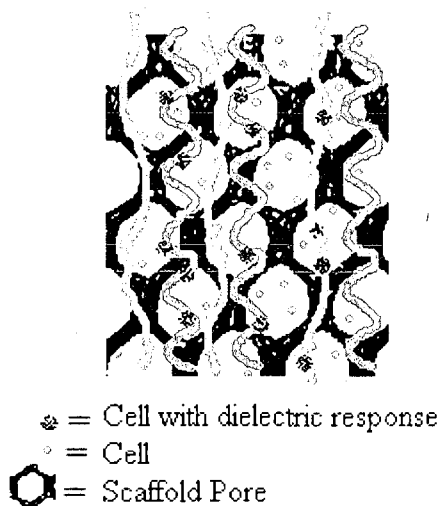
Figure 25: Long and short wavelength interaction inside a seeded scaffold.

Engineered tissues are essentially the same as naturally occurring tissue except for

the artificial ECM and the cellular density. With a nonconductive or minimally

conductive scaffold, EIS on engineered tissues should be equivalent to EIS on excised

tissue samples. Impedance analysis of tissue accounts for current travel through the

extracellular fluid and the cells. Likewise, engineered tissue EIS will account for the cell

suspension media, physiologically similar to the extracellular media, accept for newly

seeded scaffolds the current passage will meet less resistance.

Impedance spectroscopy has already been used as an on line monitoring solution

for seeded scaffolds. The faradic and non-faradic charge transfer mechanisms in

cardiomyocytes were assessed by EIS. In this case, EIS was used to evaluate the functionality of the cells, which, if in working condition, have a varying potential [88]. EIS can also be used to evaluate cellular differentiation. As mesenchymal stem cells (MSCs) differentiate, their morphology shifts accordingly. By removing background data, the differences from cell type can be noted. In addition to variations in cell morphology, changes in cell volume can be reasonably assessed by EIS as confirmed by a DNA assay. Produced proteins for the newly developing ECM can be accounted for both as a change in volume and from the polarization of the macromolecules [58, 89]. The goal of this experimental set is to demonstrate the effectiveness of EIS for determining cell and protein inside of chitosan scaffolds nondestructively.

5.2 **Materials and Methods**

5.2.1 **Preliminary Testing and Design Performed with Laura Place**

Preparation of Chitosan Scaffold

2% (wt/vol) chitosan scaffolds were prepared under the standard protocol as previously described and cast into a 4 cm specimen container.

Testing Chitosan Scaffold for Media Uptake and Particle Accumulation

Previously weighed scaffolds were soaked in complete media until saturated. Half of the scaffolds were kept saturated for 6 hours without current and the second half were treated with current. The scaffolds were weighed after the treatment and then re-lyophilized. The dry samples were then examined with SEM.

Cell Culture

Established fibrochondrocytes (ATCC, Manassas, VA) were cultured under standard conditions using Dulbeccos Modified Eagles Medium (DMEM) supplemented with 10% fetal bovine serum (FBS), 1% 4mM L-glutamine, and 1% pen strep antibiotics. Each culture was maintained in an incubator at 37°C at 5% CO_2.

Seeding Cells onto the Scaffold

The scaffold was sealed and attached to the bottom of the plexiglass box used for the particle treatment protocol. All equipment was then placed under UV light to sterilize. After sterilization, the scaffold was swelled incrementally with media. Cell suspension from a passage of the fibrochondrocytes was then placed onto the top of the scaffold. The plexiglass box and scaffold was put into a sterile plastic zippered bag and incubated overnight. After 18 hours, the chamber was moved from the incubator and placed in the cell culture hood. Prior to electrical treatment ~20 ml of fresh media was added.

Electrical Treatment

The same radial electrode set up used for the particle treatment was used on half of the scaffolds submerged in complete media. All set ups were maintained at 37° C in a water bath under the hood. The three experimental setups were: No current, positive on the inside with negative on the outside, and negative on the inside with positive on the outside. A DC power source was run at 4 V and monitored with a digital multimeter for 6 hours and a current of .015 mA. The system was then run at these conditions for 6 h.

Pico Green DNA Assay

The treated scaffold was cut into three layers and three segments of each layer in order to distinguish between the top, middle, bottom, left, right, and center. Each of the nine pieces of scaffold was stained with pico green, a DNA only stain, and placed on a slide for viewing. Pico green was chosen for its DNA exclusive binding which would prevent possible background staining of the scaffold. The samples were then observed under a fluorescence microscope and a picture was taken using Rincon software. The cells in each image were then counted and averaged. This assay was performed on all three experimental setups and on a control scaffold with no cells.

5.2.2 Scaffold Fabrication

Chitosan scaffolds were fabricated by dissolving 2 % (wt/vol) chitosan powder from crab shells in 2 % (vol/vol) acetic acid (all from Sigma, St. Louis, MO) heated to 50°C. This procedure was repeated from previous protocols which resulted in well characterized scaffolds. The chitosan solution was cast into a polyethylene specimen container to an approximate fill level of 3 cm high and frozen at -20°C for 24 hours. Once thoroughly frozen, the scaffold was lyophilized for 24 to 36 hours resulting in a foam-like 3D matrix. The sample was ensured to be completely dry by piercing the center of the scaffold with a 20 gauge needle in order to feel for irregularities indicative of insufficient freeze drying. A total of six scaffolds were fabricated from three separate batches allowing for up to 6 seedings and subsequent evaluation. Each individual scaffold was maintained in its cast shape and unaltered prior to seeding as well as stored with desiccant. Immediately prior to cell seeding, the bottom and sides were coated in paraffin

to prevent current leakage during later EIS testing. The wax coating had to be performed prior to the introduction of media but is apparently unharmful to the process.

5.2.3 Cell Culture

3T3 fibroblasts (ATCC) were thawed using the manufacturer's instructions and cultured in 25 cc culture flasks with 90% Dulbecos modified eagle media (DMEM)/ 10% fetal calf serum (FCS) (both from ATCC). Fibroblasts were chosen as the model cell due to their durability, adhesion dependence, and rapid proliferation. All flasks were maintained in the incubator at 37° C and 5% CO_2. Each flask was fed every 2 to 3 days and at approximately 75% confluency the cells were passaged. During passaging, the media was removed and the flask rinsed with PBS. The cells were trypsinized with 0.2% trypsin and a portion of the cell suspension was placed in a new flask along with fresh media to proliferate. Cells were passaged every 4 to 5 days until the cells demonstrated good morphology. On passages 3 and 4, a portion of the subculture cell suspension was retained for seeding purposes.

5.2.4 Cell Seeding

Four scaffolds, only two from the same batch, with partial wax coating were sealed to the bottom of a modified sample container with additional wax and placed under UV light for 2 hours in order to sterilize the set up. Complete media was added incrementally to the scaffold allowing it to swell until reaching full saturation at approximately 10 ml over 10 minutes time. A portion of the cell suspension acquired by subculture of the flask was added to the exposed top of the scaffold making sure to distribute the suspension evenly. Approximately 1×10^6, counted with a hemacytometer, cells were used for each scaffold. The seeded scaffold and set up were placed inside of a

sterilized zipper bag and placed inside of the 37° C/ 5% CO_2 incubator for 12 to 16 hours. Upon complete seeding, the scaffold could be removed entirely from the set up or the set up could be modified for the testing.

5.2.5 Electrical Impedance Spectroscopy (EIS)

The four scaffolds which had previously been coated in wax and implanted with cells were first run at 0.1mA from 10^{-3} to 10^3 Hz. Following the initial data set, each was subsequently run from 10^3 to 10^6 Hz and finally to the limitations of the impedance device, 10^{7}. EIS was performed on the scaffold samples using 6Al 4V ELI medical grade titanium straight wire probes (Small Parts, Inc, Miramar, FL) attached to an impedance analyzer (Solartron, 1260A, Hampshire, England). This approach has previously been used to characterize chitosan scaffolds and has been shown to be effective and non destructive. The two remaining scaffold were swollen with complete media and used as background for comparison with the seeded scaffolds. Each of the background scaffolds were run with the same current and frequency sets as the seeded. To test the strength of the protein response, FBS was added to one of the background scaffolds following initial testing in increasing increments of 10% (vol/vol) to a total of 50%.

5.2.6 Data Analysis

By plotting the real versus imaginary impedance values acquired for all samples in a Nyquist plot the impedance values were compared. Bode plots were also created for all samples in order to determine a frequency response.

5.3 <u>Results and Discussion</u>

<u>Preliminary Results Acquired with Laura Place</u>

Elemental analysis from the SEM showed that in addition to the carbon and oxygen found natively in the scaffold the complete media left traces of sodium, chlorine, and calcium. The concentrations of the trace elements were consistent for both the electrically treated and nontreated scaffolds. This consistency indicates that the electrical treatment is not causing an increased concentration of minerals inside the scaffold due to the application of current.

The pico green assay (Figure 26) showed the averages of the cell counts (Figure 27) from each of the segments were evenly distributed and maintained following both current protocols. All experiments yielded a similar numbers of cells in each scaffold as well as showing consistent seeding behavior. The consistent distribution indicates that the current didn't influence cellular migration.
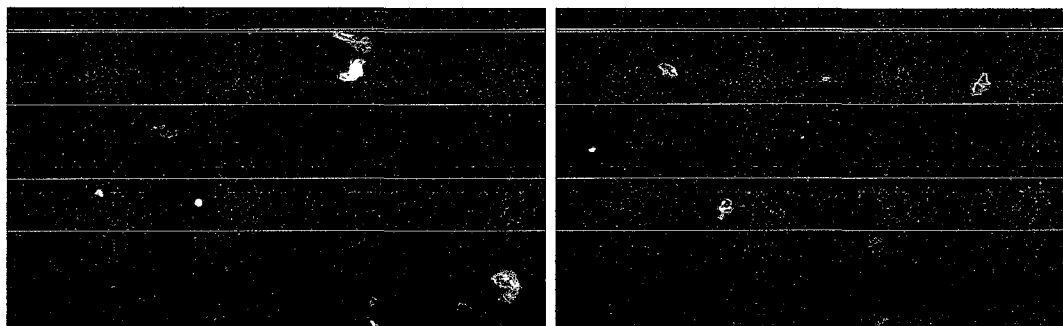
Figure 26: Representative images from fluorescence microscopy of pico green assay on seeded chitosan scaffolds (both images from middle portions of the scaffold) at 40X magnification.

This distribution most likely occurred because an electric field of 2.67 V/cm was used to treat these scaffolds, and in previous experiments cells were not seen to migrate with preference for the cathode until the field reached 5 V/cm [90]. There is also no negative effect on cell population when the electrical treatment is used, thus the field may be used for other purposes without fear of damaging the cells.
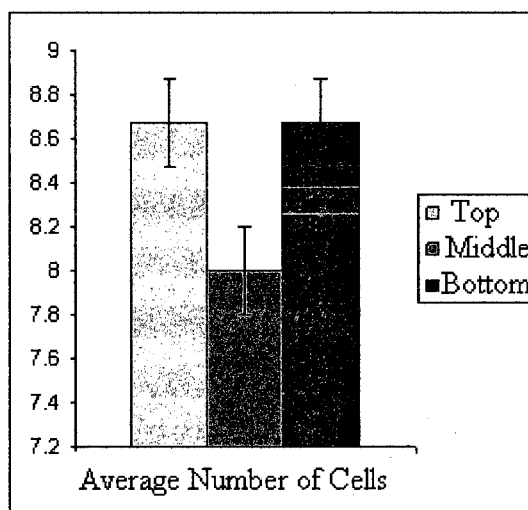
Figure 27: Average cell count per regional sectioning of a chitosan scaffold 18 hours after seeding (n=8).

Bode plots showed the typical signal time constant formation. In the α dispersion, the Nyquist plots of the unseeded scaffolds showed very similar curvature and resistance to the previously reported values for unmodified scaffolds saturated with PBS. This correspondence is reasonable since both the PBS and the media have very similar ionic concentration and the lower frequency ranges primarily affect ion transport. When the seeded scaffold were plotted along side the unseeded scaffold in the α dispersion, there was no notable difference between them. This result may be an indication that the total cell volume contained within the scaffold was not enough to impede current in the

scaffold. The single semi circle likely indicates that there is not a significant contribution from the gap junctions on the fibroblasts (Figure 28).
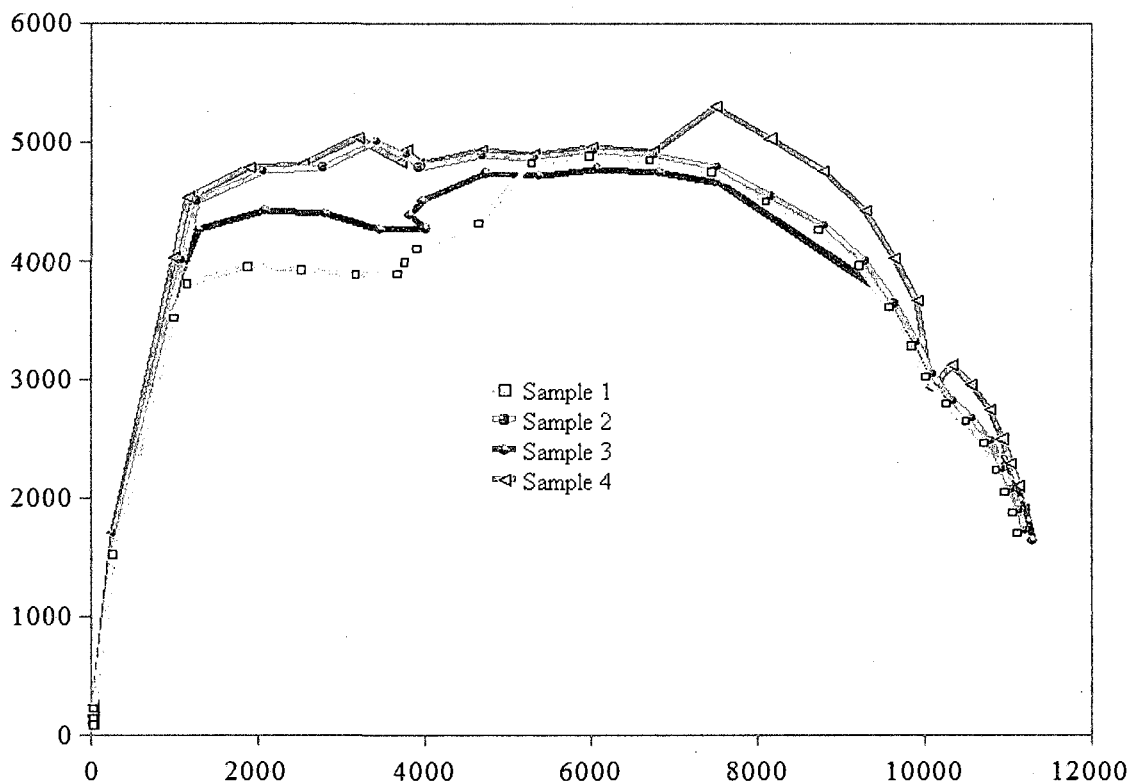
Figure 28: Nyquist plot of the real vs. imaginary impedance of seeded scaffolds (Sample 1-3) and the background scaffold (sample 4) tested in the α dispersion.

Once analyzed in the β dispersion, the unseeded scaffold showed a small cluster of points associated with the highest frequencies on the cusp of the γ dispersion. Upon isolation the high frequency points (Figure 29), may be an indicator of protein polarization. The high frequency values increased with an addition of 30% more vol/ vol fetal bovine serum. The seeded scaffold showed a corresponding cluster at high frequencies but no pattern for the impedance could be associated with the cells. It is

possible that the quantity of cells was insufficient to see a significant difference as compared to the volume of media present.
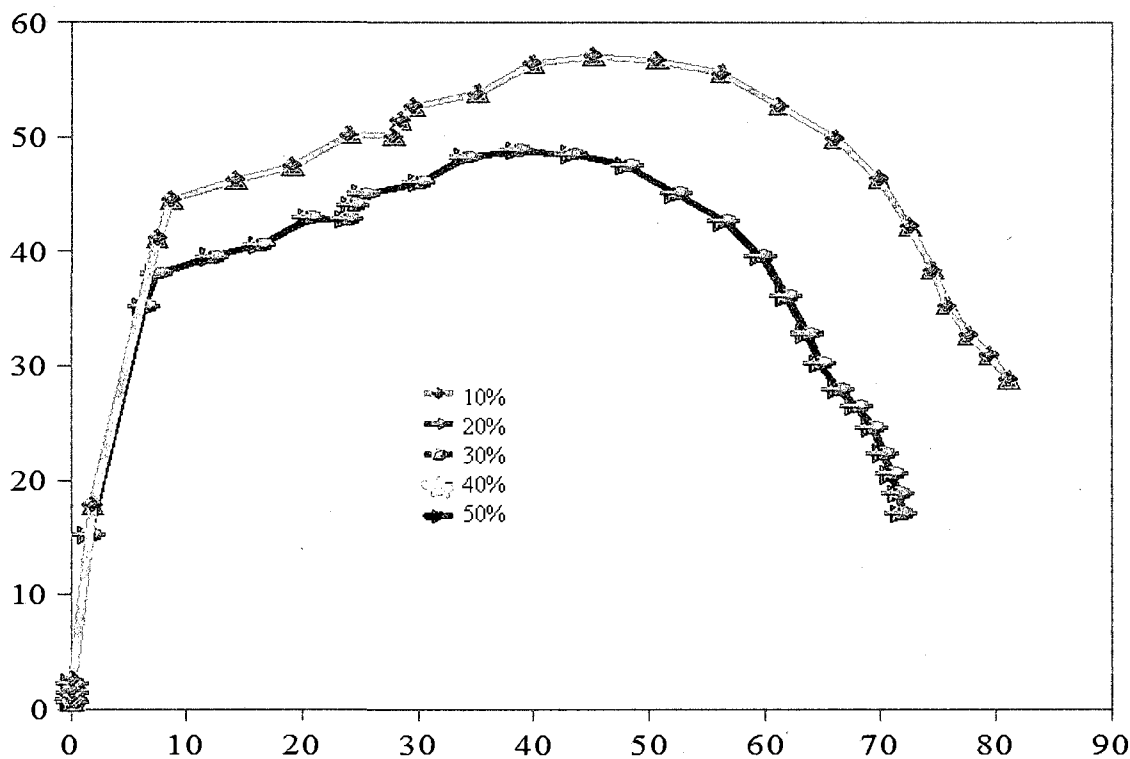
Figure 29: Subset Nyquist plot from the β and γ dispersion cusp showing protein response from the addition of fetal bovine serum.

5.4 Conclusions

Positive results from the pico green assay show that the cell seeding procedure works for chitosan scaffolds; however, the β dispersion data did not indicate a cellular capacitive effect and the α dispersion did not show a change in scaffold porosity from the cell volume. Reasonably, the capacitor effect from the cells may be masked by the overall impedance of the engineered tissue as a whole. In regards to the standard model circuit (Figure 30), reasonable comparative values can be assigned to the circuit components. The extracellular resistance will remain low on newly seeded scaffolds.

With an average cell diameter of 10 μm and a chitosan pore size of approximately 100 μm, the volume difference between cell volume and the pore volume is substantial so the number of cells required to increase the impedance of the system in the α dispersion will either require an initially prohibitive cell seeding population or time for the cells to proliferate. Also, if the cells had failed to attach to the scaffold, lack of adhesion leads to a round profile which minimizes the accessible surface area seen by the directional electric field. The circuit elements associated with the cells will be masked by the background resistor until the cell population is once again quite large. In regards to the circuit as a whole, current introduced into the scaffold will initially by pass the cell components because of their inherent high resistance and the extracellular fluid, the media, will be the path of least resistance.
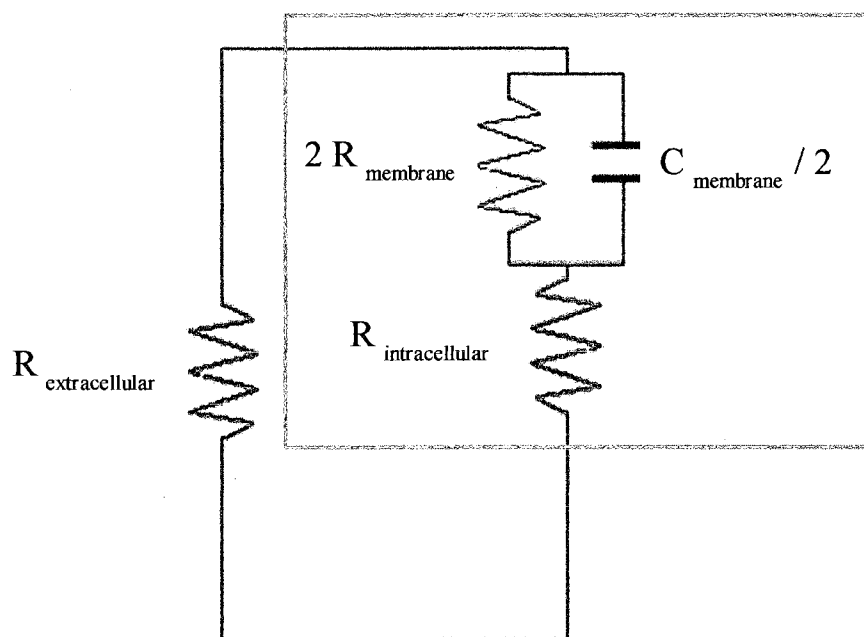
Figure 30: Model circuit for electrochemical impedance spectroscopy in tissue with cell related components in light grey box.

It is possible that an increase in cell population might deliver a stronger signal. The small but notable reaction of the protein to high frequency stimulation is further validated by the increase in magnitude with the increase in protein concentration. This result suggests that a correlation between impedance values and protein concentration could be established as an evaluation protocol at minimum for the increase in protein concentration associated with ECM production and gene expression.

CHAPTER 6

CONCLUSIONS AND FUTURE WORK

6.1 Characterization

In comparison to the more commonly used characterization techniques for tissue engineering scaffolds, the data acquired and interpreted from the EIS compares favorably with the added benefit of maintaining the physical and chemical parameters of the scaffold. Porosity and pore connectivity values are critical assessments to judge both the quantity and evenness in pore structure. In scaffolds with traditionally regular pore structure, subtle variations can be detected with EIS testing. Unlike other characterization methods, EIS not only does not damage the scaffold but also maintains the pore fluid presence. By not displacing or modifying the pore fluid, modifications made to the scaffold can also be evaluated without removal, a benefit over other practiced nondestructive approaches. Additionally, EIS can be performed in a short period of time. With most porosity measurements taking less than an hour in total, EIS has the strong possibility of being an efficient evaluation technique in a mass production style setting. In all, the comparison performed indicates that the EIS provides an effective non-destructive way of characterizing the physical properties of the chitosan scaffold under physiologically relevant conditions.

6.2 Modification

The electrokinetic intrusion was determined to be successful for the modification of chitosan scaffolds when the particles are in the 15 μm arena as compared to simple exposure to the particle suspension without the potential difference. Previous attempts at scaffold modification with micron sized particles showed that their incorporation during the fabrication stage resulted in compromised structure which then leads to compromised scaffold functionality. While the passive incorporation of nanoparticles has been effectively demonstrated, the interaction between cells and influential materials has been shown to be size dependent [91]. This size dependence necessitates modification with micron size particles.

Larger particles in the ~100 μm range proved less successful with electrokinetic modification and the length of time required is prohibitive. Past the nanoscale, particles will not be incorporated into the cell. Instead, the surface area of the particle is the source of interaction. Therefore, the larger particles can be partially disregarded because their effect will be the same as smaller microparticles due to their size comparison to cells. The successful electrokinetic incorporation of the 10 to 20 μm particle range at low voltage, within physiologically acceptable parameters, showed that the desired modification could be achieved subsequent to cell seeding. Also, evaluation of the modified scaffold with EIS showed potential for characterization without altering the modification.

6.3 <u>Cell Monitoring</u>

The final stage in the construction of an engineered tissue is the assessment of tissue viability which is not only the viability and expression of the cells but also the development of a natural ECM and the removal of the scaffold. Engineered tissue assessment is often done in the same manner as normal tissue histology where excised segments are stained for each component. This kind of staining prohibits the use of the tissue and can only be performed once which prohibits the observation of remodeling. EIS has been effectively used for tissue characterization and, in limited cases, for cell characterization in engineered tissues. With a proven cell seeding protocol, it seems likely that a volume and cell capacitor response could be acquired in an established cell embedded scaffolds. Once the cells are established, the capacitor effect from the cells should be notable. An increase in cell population should not only deliver a stronger capacitor signal but also leader to a greater protein concentration which has already been identified in chitosan scaffolds. The change in protein concentration and variation in extracellular resistance, based on volume and composition, are both indicative of remodeling within the engineered scaffold. By combining these electrical responses, EIS has potential for characterizing and online monitoring of engineered tissues.

6.4 <u>Summation</u>

Completion of the three experimental sets suggested a positive correlation between the techniques implemented and intended results. EIS was cable of assessing the engineered tissue from construction of the scaffold, following modification, and subsequent to cell seeding without destroying of altering the tissue components.

Additionally, the electrokinetic incorporation demonstrates the capability of the approach for modification with charged particles without damaging the scaffold or compromising functionality both prior to and following cell seeding. Overall, there is potential for electrokinetics in the characterization, modification, and long-term evaluation of scaffolds for tissue engineering.

6.5 Future Work

6.5.1 Characterization

To further validate the results of the characterization experiments, scaffolds of varying composition and porosity should be tested with EIS. For large scale production, designing a testing container that would prevent current leakage without modifying the scaffold at all could increase the rate of testing.

6.5.2 Modification

By varying the size of the particles within the range from 1 μm to 50 μm, the size limitations of the electrophoretic technique can be more clearly determined. Expansion on the size range and charge of particles will also allow for better modeling of electrophoretic rate and mass transported. Modification of charge on uniformed sized particles will help facilitate this modeling and potentially improve the motility of the particles. Once a true size range has been determined, nonmodifying particles should be coated with growth factors and then electrophoretically transported. Finally, particles should be eletrophoretically transported into cell seeded scaffolds to confirm that modifications can be made in the presence of cells.

6.5.3 <u>Online Monitoring</u>

Increasing the number of cells implanted will be the first step in identifying the most usable frequency range to balance exposure time with usable data. Subsequent, cell experiments should be performed with cells of different phenotypes to determine working parameters of long term engineered tissue evaluation. Upon completion of the alternate phenotype EIS evaluations, average resistance and capacitance values can be determined based on cell number. From these values, model circuits can be made and confirmed for each cell type therefore providing a method for determining ideal results and comparing them to acquired values over time.

APPENDIX A

PROCEDURES FOR SCAFFOLD FABRICATION, MERCURY INTRUSION POROSIMETRY, AND ELECTROCHEMICAL IMPEDANCE SPECTROSCOPY

Chitosan Scaffold Fabrication

1. Create a 2% (vol/vol) solution of acetic acid in deionized water, approximately 30 ml per scaffold

2. Weigh out 2% (wt/ vol) chitosan powder (sigma Aldrich, St. Louis, MO) for the intended volume.

3. Heat the dilute acetic acid to 50 C with a watch glass covering to prevent loss due to evaporation.

4. While magnetically stirring, slowly add the chitosan to the acetic acid solution waiting in between allotments for the powder to dissolve.

5. Stirring should be done at the lowest reasonable speed to prevent the generation of air bubbles. The rate will have to be increased as the amount of chitosan in solution increases and the solution becomes more viscous.

6. Once all of the chitosan has been dissolved the stir bar can be removed, and the solution poured into the casting containers, approximately 20 to 25 ml total.

7. Each container of chitosan solution is frozen at -20 C for a minimum of 12 hours.

8. The containers of frozen solution are removed and a lid with a ~ 5mm hole is placed on top prior to their placement in the lyophilizer.

9. All frozen solutions are lyophilized for 24 to 36 hours and pierced with a 22 gauge needle upon removal to insure thorough freeze drying.

10. Complete scaffolds are stored on desiccant to prevent their decay prior to use.

Mercury Intrusion Porosimetry

1. A desiccated sample was weighed and placed inside of a powder sample penetrometer (Micromeritics Autopore IV, Norcross, GA).

2. The cap was sealed with vacuum grease and the penetrometer placed in the low pressure portal of the porosimeter (Micromeritics Autopore IV, Norcross, GA).

3. The weight of the sample was entered into the Autopore program as well as the contact angle and surface tension of the mercury to be used.

4. Using the automatic macropore setting provided by the manufacturer, low pressure analysis was performed resulting in an approximated pore diameter provided by the software.

5. The penetrometer is removed and weighed. Because the weight of the empty penetrometer and dry sample are known, the difference in weight is attributed to the mercury. By dividing the weight of the mercury by it's density at room temperature, the volume can be determined. The volume of the penetrometer is known, so the difference between the volume without the scaffold and the volume containing the scaffold is the total volume of the solid component of the scaffold. The software determines the total intrusion volume per gram of the sample which can then be multiplied by the weight of the original sample to determine the scaffold pore volume.

6. The scaffold pore volume (vol_{in}) over the solid volume (vol_{scf}) plus the pore volume yields the porosity (Φ)

$$\Phi = \frac{vol_{in}}{vol_{in} + vol_{scf}}.$$
[A.A.1]

Electrochemical Impedance Spectroscopy

1. Scaffolds were coated on the bottom and sides with a layer of paraffin wax and sealed inside the original casting container. The wax seal prevents current leakage.

2. Two titanium wire probes were inserted at ~1 cm (later measured with a micrometer) and maintained at that distance by drilling corresponding holes in the lid.

3. Each scaffold was swollen with PBS in increments of 1 ml per minute until totally saturated.

4. Alligator clips were used to attach to impedance analyzer (Solartron, 1260A, Hampshire, England) leads to the titanium probes.

5. In the provided Z Plot software, a constant current of 0.1 mA was set. The desired frequency set was input at which point the impedance analysis began at each point of the sweep.

6. Output was provided in terms of the real impedance, imaginary impedance, the impedance magnitude, and the phase shift for each frequency value.

APPENDIX B

CALCULATION OF POROSITY FROM ELECTROCHEMICAL
IMPEDANCE SPECTROSCOPY NYQUIST PLOT

Bulk resistance (R_b) was approximated to be 10,600 ohms from the Nyquist Plots generated from EIS of the 5 unmodified scaffolds. Titanium electrodes with outer diameters (d) of 1.27×10^{-4} m were used and the surface area (S) calculated using the inserted height (h) of 8.60×10^{-3} m

$$S = d\pi \cdot h = (1.27 \times 10^{-4}\pi) \cdot 8.60 \times 10^{-3} = 3.4295 \times 10^{-6} m^2. \quad \text{[A.B.1]}$$

The entire surface area of the electrode does not contribute to the electric field between the electrodes (Figure 31).
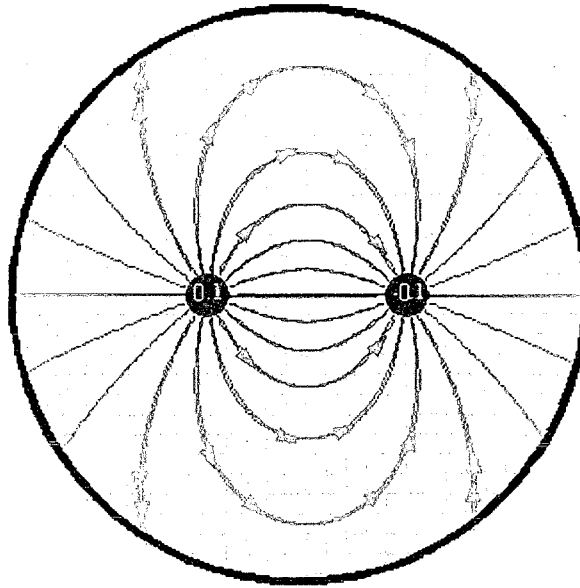
Figure 31: Electric field paths for 0.1mA current applied to parallel electrodes ~1 cm in a cylindrical sample container.

Consequently, the effective surface area (A) was approximated to be half of the total surface area

$$A = 0.5 \cdot S = 0.5 \cdot 3.4295 \times 10^{-6} = 1.7148 \times 10^{-6} m^2. \quad \text{[A.B.2]}$$

With each electrode separated by a length (l) of 1.10x10-2, the effective conductivity (σ_{eff}) was determined

$$\sigma_{eff} = \frac{l}{R_b A} = \frac{1.10 \times 10^{-2}}{10,600 \cdot 1.7148 \times 10^{-6}} = .605 Sm^{-1}.$$

[A.B.3]

The previously reported and confirmed value for the conductivity of PBS (σ_0), 1.2 Sm^{-1}, was used to determine porosity (Φ) via Archie's law where the saturation constant (C) and the cementation factor (m) implemented

$$\Phi_0 = \left(\frac{\sigma_{eff}}{C\sigma_0}\right)^{\frac{1}{m}} = \left(\frac{.605}{1 \cdot 1.2}\right)^{\frac{1}{2}} = .7102 = 71.02\% \approx 71.0\%.$$

[A.B.4]

Calculations for the porosity of the iron oxide treated samples were based on an estimated R_b of 10,850 ohms with the same geometric values. Effective conductivity was determined

$$\sigma_{eff} = \frac{l}{R_b A} = \frac{1.10 \times 10^{-2}}{10,850 \cdot 1.7148 \times 10^{-6}} = .591 Sm^{-1}.$$

[A.B.5]

From the determined effective conductivity, the porosity was calculated

$$\Phi_0 = \left(\frac{\sigma_{eff}}{C\sigma_0}\right)^{\frac{1}{m}} = \left(\frac{.591}{1 \cdot 1.2}\right)^{\frac{1}{2}} = .7017 = 70.17\% \approx 70.2\%.$$

[A.B.6]

APPENDIX C

POSTERS AND PRESENTATIONS

1. S. Tully, "Cellular Cytoskeletal Response Studied by AFM," *Biomedical Research Symposium at Louisiana Tech*, May 6, 2005.

2. S. Tully, H. E. Cardenas and P. S. Sit, "Effect of Ionic Concentration on Chitosan Scaffold Characteristics Measured by Electrochemical Impedance Spectroscopy," *Houston Society for Engineering in Medicine and Biology*, February 8-9, 2007.

3. S. Tully, H. Cardenas, P. S. Sit, "Effect of Ionic Concentration on Chitosan Scaffold Characteristics Measured by Electrochemical Impedance Spectroscopy," *Annual Meeting of the Society for Biomaterials*, April 18-21, 2007.

4. S. Tully, H. Cardenas, P. S. Sit, "Pore Geometry Characterization of Chitosan Scaffolds: A Comparison Study Among Techniques," Biomedical Engineering Society Meeting, October 2-4, 2008.

5. S. Tully- Dartez, H. Cardenas, P. S. Sit, "A Comparison Study Among Characterization Methods for the Pore Geometry of Chitosan Scaffolds," *Houston Society for Engineering in Medicine and Biology,* March 19-20, 2009.

6. S. Tully- Dartez, H. Cardenas, P. S. Sit, "A Comparison Study Among Characterization Methods for the Pore Geometry of Chitosan Scaffolds," *Society for Biomaterials,* April 22-25, 2009.

REFERENCES

[1]   L. A. Siminoff, R. M. Arnold, A. L. Caplan, B. A. Virnig, D. A. Seltzer, "Public Policy Governing Organ and Tissue Procurement in the United States," *Annals of Internal Medicine,* vol. 123, pp. 10-17, 1995.

[2]   "2007 Annual Report of the U.S. Organ Procurement and Transplantation Network and the Scientific Registry of Transplant Recipients: Transplant Data 1997-2006," H. R. a. S. Administration, Ed. Rockville, MD: Healthcare Systems Bureau, Division of Transplantation, 2007.

[3]   K. Solez, L. C. Racusen, M. E. Billingham, *Solid Organ Transplant Rejection: Mechanisms, Pathology, and Diagnosis*, 1 ed. New York: Informa HealthCare, 1996.

[4]   E. Sachlos, J.T. Czernuszka, "Making Tissue Engineering Scaffolds Work. Review: The application of solid freeform fabrication technology to the production of tissue engineering scaffolds," *Eur Cell Mater,* vol. 5, pp. 29-40, 2003.

[5]   P. A. Gunatillake, R. Adhikari, "Biodegradable synthetic polymers for tissue engineering," *European Cells and Materials,* vol. 5, pp. 1-16, 2003.

[6]   F. Wang, L. Shor, A. Darling, S. Khalil, W. Sun, S. Guceri, A. Lau, "Precision extruding deposition and characterization of cellular poly-caprolactone tissue scaffolds," *Rapid Prototyping Journal,* vol. 10, pp. 42 - 49, 2004.

[7]   T. Karande, J. L. Ong, C. M. Agrawal, "Diffusion in Musculoskeletal Tissue Engineering Scaffolds: Design Issues Related to Porosity, Permeability, Architecture, and Nutrient Mixing," *Annals of Biomedical Engineering,* vol. 32, pp. 1728-1743, 2004.

[8]   J. Guana, K. L. Fujimotoa, M. S. Sacksa, W. R. Wagne, "Preparation and characterization of highly porous, biodegradable polyurethane scaffolds for soft tissue applications," *Biomaterials,* vol. 26, pp. 3961-3971, 2005.

[9]   L. Safinia, A. Mantalaris, A. Bismarck, "Nondestructive technique for the characterization of the pore size distribution of soft porous constructs for tissue engineering.," *Langmuir,* vol. 22, pp. 3235-3242, 2006.

[10] S. Kim, Chu C, "Pore structure analysis of swollen dextran-methacrylate hydrogels by SEM and mercury intrusion porosimetry," *Journal of Biomedical Materials Research,* vol. 53, pp. 258-266, 2000.

[11] D. W. Hutmacher, "Scaffolds in tissue engineering bone and cartilage," *Biomaterials,* vol. 21, pp. 2529-2543, 2000.

[12] J. L. Drury, D. J. Mooney, "Hydrogels for tissue engineering: scaffold design variables and applications " *Biomaterials,* vol. 24, pp. 4337-4351 2003.

[13] L. Lu, X. Zhu, R. G. Valenzuela, B. L. Currier, M. J. Yaszemski, "Biodegradable polymer scaffolds for cartilage tissue engineering," *Clinical Orthopedics Relat Research,* vol. 391, pp. 251-70, 2001.

[14] G. Chen, T. Ushidaa, T. Tateishia, "Development of biodegradable porous scaffolds for tissue engineering," *Materials Science and Engineering: C* vol. 17, pp. 63-69, 2001.

[15] M. Lopez-Heredia, P. Weiss, P. Layrolle, "An electrodeposition method of calcium phosphate coatings on titanium alloy," *Journal of Materials Science: Materials in Medicine,* vol. 18, pp. 381-390, 2007.

[16] M. H. Sheridan, L. D. Shea, M. C. Peters, D. J. Mooney, "Bioabsorbable polymer scaffolds for tissue engineering capable of sustained growth factor delivery," *Journal of Controled Release,* vol. 64, pp. 91-102, 2000.

[17] Y. Liu, E. B. Hunziker, P. Layrolle, J. D. De Bruijn, K. De Groot, "Bone Morphogenetic Protein 2 Incorporated into Biomimetic Coatings Retains Its Biological Activity," *Tissue Engineering,* vol. 10, pp. 101-108, 2004.

[18] P. K. Chu, J. Y. Chena, L. P. Wanga, N. Huangb, "Plasma-surface modification of biomaterials," *Materials Science and Engineering,* vol. 36, pp. 143-206, 2002.

[19] L. Weiss, *Cell and tissue biology, a text book of histology* Baltimore, MD: Urban & Schwarzenberg, 1983.

[20] E. Claridge, S. Cottonb, P. Hallc, M. Moncrieffd, "From colour to tissue histology: Physics-based interpretation of images of pigmented skin lesions," *Medical Image Analysis,* vol. 7, pp. 489-502, 2003.

[21] S. H. Han, Y. H. Kim, M. S. Park, I. A. Kim, J. W. Shin, W. I. Yang, K. S. Jee, K. D. Park, G. H. Ryu, J. W. Lee, "istological and biomechanical properties of regenerated articular cartilage using chondrogenic bone marrow stromal cells with a PLGA scaffold in vivo," *Journal of Biomedical Materials Research: Part A,* vol. 87A, pp. 850-861, 2008.

[22] Y. Q. Zhang, W. J. Zhang, W. Liu, X. J. Hu, G. D. Zhou, L. Cui, Y. Cao, "Tissue Engineering of Corneal Stromal Layer with Dermal Fibroblasts: Phenotypic and Functional Switch of Differentiated Cells in Cornea," *Tissue Engineering: Part A*, vol. 14, pp. 295-303, 2008.

[23] Y. Yang, H. P. Yiu, A. J. El Haj "On-line fluorescent monitoring of the degradation of polymeric scaffolds for tissue engineering," *Analyst*, vol. 130, pp. 1502-06, 2005.

[24] J. Polak, S. Mantalaris, S. E. Harding, "Advances in Tissue Engineering " London: Imperial College Press, 2008, p. 948.

[25] S. H. E. Nettles D.L., J. A. Gilbert, "Potential use of chitosan as a cell scaffold material for cartilage tissue engineering.," *Tissue Engineering*, vol. 8, pp. 1009-16, 2002.

[26] W. Suphasiriroj, P. Yotnuengnit, R. Surarit, R. Pichyangkura, "The fundamental parameters of chitosan in polymer scaffolds affecting osteoblasts (MC3T3-E1) " *Journal of Materials Science: Materials in Medicine*, vol. 20, pp. 309-320, 2009.

[27] S. V. Madihally, H. W. Matthew, "Porous chitosan scaffolds for tissue engineering," *Biomaterials*, vol. 20, pp. 1133-42, 1999

[28] S. H. Elder, D. L. Nettles, J. D. Bumgardner, "Biopolymer Methods in Tissue Engineering." vol. 238 Totawa, NJ: Humana Press, 2004.

[29] W. W. Thein-Han, Y. Kitiyanant, R. D. K. Misra, "Chitosan as Scaffold Matrix for Tissue Engineering," *Materials Science and Technology*, vol. 24, pp. 1062-1075, 2008.

[30] W. C. Hsieh, C. P. Chang, S. M. Lin, "Morphology and characterization of 3D micro-porous structured chitosan scaffolds for tissue engineering," *Colloids and Surfaces B: Biointerfaces*, vol. 57, pp. 250-255, 2007.

[31] P. J. Van deVord, H. W. Matthew,S. P. DeSilva, L. Mayton, B. Wu, P. H. Wooley, "Evaluation of the biocompatibility of a chitosan scaffold in mice," *Journal of Biomedical Materials Research*, vol. 59, pp. 585-90, 2002.

[32] D. Griffon, M. R. Sedighi, D. V. Schaefer, J. A. Eurella, A. L. Johnson, "Chitosan scaffolds: Interconnective pore size and cartilage engineering," *Acta Biomaterialia*, vol. 2, pp. 313-20, 2006.

[33] M. Lei, S. Q. Liu, Y. L. Liu, "Resveratrol protects bone marrow mesenchymal stem cell derived chondrocytes cultured on chitosan-gelatin scaffolds from the inhibitory effect of interleukin-1beta.," *Acta Pharmacol Sin*, vol. 29, pp. 1350-6, 2008.

[34] A. R. Costa-Pinto, A. J. Salgado, V. M. Correlo, P. Sol, M. Bhattacharya, P. Charbord, R. L. Reis, N. M. Neves, "Adhesion, proliferation, and osteogenic differentiation of a mouse mesenchymal stem cell line (BMC9) seeded on novel melt-based chitosan/polyester 3D porous scaffolds.," *Tissue Engineering: Part A,* vol. 14, pp. 1049-57, 2008.

[35] M. H. Cho, K. S. Kim, H. H. Ahn, M. S. Kim, S. H. Kim, G. Khang, B. Lee, H. B. Lee, "Chitosan gel as an in situ-forming scaffold for rat bone marrow mesenchymal stem cells in vivo," *Tissue Engineering: Part A,* vol. 14, pp. 1099-108, 2008.

[36] Y. Wan, A. Yu, H. Wu, Z. Wang, D. Wen, "Porous-conductive chitosan scaffolds for tissue engineering II. in vitro and in vivo degradation," *Journal of Material Sciences: Materials in Medicine,* vol. 16, pp. 1017-28., 2005.

[37] M. H. Hoa, D. Wanga, H. Hsieha, H. Liub, T. Hsienc, J. Laid, L. Houe, "Preparation and characterization of RGD-immobilized chitosan scaffolds," *Biomaterials,* vol. 26, pp. 3197-3206, 2005.

[38] G. Medrado, C. B. Machado, P. Valerio, M. D. Sanches, A. M. Goes, "The effect of a chitosan/gelatin matrix and dexamethasone on the behavior of rabbit mesenchymal stem cells," *Biomedical Materials,* vol. 3, pp. 155-161, 2006.

[39] U. Masaki, J. Yi, N. Hideshi, K. Daisuke, S. Kenji, M. Yasunori, "Introduction of poly-L-lactic acid microspheres into the skin using supersonic flow: effects of helium gas pressure, particle size and microparticle dose on the amount introduced into hairless rat skin," *The Journal of pharmacy and pharmacology* vol. 54, pp. 781-90, 2002.

[40] J. C. Rawlins, *Basic AC Circuits,* St. Louis, MO: Elsevier Science & Technology Books, 2000.

[41] J. R. Scully, D. C. Silverman, M. W. Kendig, *Electrochemical Impedance: Analysis and Interpretation.* West Conshohocken, PA: ASTM International, 1993.

[42] J. Reynolds, *An introduction to applied and environmental geophysics.* Hoboken, NJ: John Wiley, 1997.

[43] G. Mavko, T. Mukerji, J. Dvorkin, *The Rock Physics Handbook: Tools for Seismic Analysis of Porous Media.* New York, NY: Cambridge University Press, 2003.

[44] J. W. Jewett, R. A. Serway, *Physics for scientists and engineers with modern physics,* 7 ed. Pacific Grove, CA: Brooks/Cole, 2007.

[45] E. M. Abousrafab, J. M. Somervillea, S. A. Hamiltona, P. W. H. Oldena, B. D. G. Smarta, J. Forda, "Pore geometrical model for the resistivity of brine saturated rocks," *Journal of Petroleum Science and Engineering,* vol. 65, pp. 113-122, 2009.

[46] Z. Deyl, F. M. Everaerts, *Electrophoresis: A Survey of Techniques and Applications, Pt. A* Elsevier Science, 1980.

[47] M. Bier, *Electrophoresis: theory, methods, and applications.* St. Louis, MO: Academic Press, 1959.

[48] R. C. Dorf, *The electrical engineering handbook.* Boca Raton, FL: CRC Press, 1997.

[49] Q. Luo, H. Wang, X. Zhang, Y. Qian, "Effect of Direct Electric Current on the Cell Surface Properties of Phenol-Degrading Bacteria," *Applied Environmental Microbiology,* vol. 71, pp. 423-427, 2005.

[50] J. Pu, M. Zhao "Golgi polarization in a strong electric field," *Journal of Cell Science,* vol. 118, pp. 1117-1128, 2005.

[51] S. D. Huelin, H. R. Baker, K. M. Poduska, E. F. Merschrod, "Aggregation and Adsorption of Type I Collagen near an Electrified Interface," *Macromolecules,* vol. 40, pp. 8440-8444, 2007.

[52] W. Saslow, *Electricity, Magnetism, and Light.* St Louis, MO: Elsevier Science & Technology Books, 2002.

[53] D. A. Deana, T. Ramanathanb, D. Machadoa, R. Sundararajan, "Electrical impedance spectroscopy study of biological tissues," *Journal of Electrostatics,* vol. 66, pp. 165-177, 2008.

[54] S. Grimnes, O. G. Martinsen, *Bioimpedance and Bioelectricity Basics.* St Louis, MO: Elsevier Science & Technology Books, 2008.

[55] M. Genescà, A. Ivorra, A. Sola, L. Palacios, J. M. Goujon, T. Hauet, R. Villa, J. Aguiló, G. Hotter, "Electrical bioimpedance measurement during hypothermic rat kidney preservation for assessing ischemic injury," *Biosensors & bioelectronics,* vol. 20, pp. 1866-71, 2005.

[56] I. O. K'Owino, O. A Sadik, "Impedance Spectroscopy: A Powerful Tool for Rapid Biomolecular Screening and Cell Culture Monitoring," *Electroanalysis,* vol. 17, pp. 2101-2113, 2005.

[57] H. H. Huang, S. J. Pam, F. H. Lu "Surface electrochemical impedance in situ monitoring of cell-cultured titanium with a nano-network surface layer," *Scripta materialia,* vol. 53, pp. 1037-1042, 2005.

[58] P. O. Bagnaninchi, M. Dikeakos, T. Veres, M. Tabrizian "Complex permittivity measurement as a new noninvasive tool for monitoring in vitro tissue engineering and cell signature through the detection of cell proliferation, differentiation, and pretissue formation," *IEEE Transactions on NanoBioscience,* vol. 3, pp. 243-250, 2004.

[59] R. Langer, J. P. Vacanti, "Tissue engineering," *Science,* vol. 260, pp. 920-926, 1993.

[60] L. L. Hench, J. M. Polak, "Third-Generation Biomedical Materials," *Science,* vol. 295, pp. 1014-17, 2002.

[61] L. G. Griffith, G. Naughton, " Tissue Engineering--Current Challenges and Expanding Opportunities," *Science,* vol. 295, pp. 1009-1014, 2002.

[62] M. Bekhit, S. A. Khalil, "Electrical Properties of Moist Limestone Samples In The Frequency Range 1Hz-10 7Hz From Abu Rawash Area," *Australian Journal of Basic and Applied Sciences,* vol. 1, pp. 741- 50, 2007.

[63] N. Neithalath, W. J. Weiss, J. Olek, " Characterizing Enhanced Porosity Concrete Using Electrical Impedance To Predict Acoustic and Hydraulic Performance," *Cement and Concrete Composites,* vol. 36, pp. 2074-2085, 2006.

[64] L. Xin, D. Xiuzhen, F. Feng, "Study on changes of characteristic parameters of biological tissues impedance spectroscopy in vitro within 5 to 360 min after excision at the frequency range from 1Hz to 1MHz," in *IEEE Engineering in Medicine and Biology 27th Annual Conference,* Shanghai, China, September 1-4, 2005, 2005, pp. 1123-1126.

[65] T. J. Shankland, "Electrical Conduction in Rocks and Minerals: Parameters for Interpretation," *Physics of the Earth and Planetary Interiors,* vol. 10, pp. 209-219, 1975.

[66] A. Malich, T. Fritsch, C. Mauch, "Electrical Impedance Scanning: a New Technique in the Diagnosis of Lymph Nodes in which Malignancy is Suspected on Ultrasound," *British Journal of Radiology,* vol. 74, pp. 42-47, 2001.

[67] P. X. Ma, J. H. Elisseeff, *Scaffolding in Tissue Engineering,* 1st ed. New York: CRC, 2005.

[68] M. Pavlin, T. Slivnik, D. Miklav, "Effective Conductivity of Cell Suspensions," *IEEE Transactions on Biomedical Engineering,* vol. 49, pp. 77-88, 2002.

[69] A. R. Hambley, *Electrical Engineering Principles & Applications,* 3rd ed. Saddle River, NJ: Prentice- Hall, 1997.

[70] F. D. Borner, "Estimation of Hydraulic Conductivity from Complex Electrical Measurements," in *SCA Conference*. vol. International SCA symposium proceedings: Society of Professional Well Log Analysts San Francisco, CA: Society of Core Analysts Chapter-at-Large, 2005, pp. 1-10.

[71] P. Wong, *Methods of the Physics of Porous Media: Experimental Methods in the Physical Sciences* vol. 35. New York: Academic Press, 1999.

[72] S. Verriera, J. Blakera, V. Maquet, L. Hencha, A. Boccaccini, "PDLLA/Bioglass® composites for soft-tissue and hard-tissue engineering: an in vitro cell biology assessment," *Biomaterials,* vol. 25, pp. 3013-3021, 2004.

[73] M. J. Kujawa, D. A. Carrino, A. I. Caplan, "Substrate-bonded hyaluronic acid exhibits a size-dependent stimulation of chondrogenic differentiation of stage 24 limb mesenchymal cells in culture.," *Developmental Biology,* vol. 114, pp. 519-28, 1986.

[74] R. S. Tıgh, A. Karakecili, "In Vitro Characterization of Chitosan Scaffolds: Influence of Composition and Deacetylation Degree," *J Mater Sci: Mater Med,* vol. 18, pp. 1665-1674, 2007.

[75] C. C. Barrias, C. C. Ribeiro, M. A. Barbosa, "Adhesion and Proliferation of Human Osteoblastic Cells Seeded on Injectable Hydroxyapatite Microspheres," *Key Engineering Materials,* vol. 254-256, pp. 877-880, 2004.

[76] P. L. Apopa, Y. Qian, R. Shao, N. L. Guo, D. Schwegler-Berry, M. Pacurari, D. Porter, X. Shi, V. Vallyathan, V. Castranova, D. C. Flynn, "Iron oxide nanoparticles induce human microvascular endothelial cell permeability through reactive oxygen species production and microtubule remodeling," in *Particle and Fibrer Toxicology*. vol. 6: Pubmed Central, 2009.

[77] H. E. Cardenas, L. J. Struble, "Electrokinetic Nanoparticle Treatment of Hardened Cement Paste for Reduction of Permeability," *Journal of Materials in Civil Engineering,* vol. 18, pp. 554-560, 2006.

[78] S. Karuppuchamy, K. Nonomura, T. Yoshida, T. Sugiura, H. Minoura, "Cathodic electrodeposition of oxide semiconductor thin films and their application to dye-sensitized solar cells," *Solid State Ionics,* vol. 151, pp. 19-27, 2002.

[79] M. Kutz, *Environmentally Conscious Materials and Chemicals Processing.* Hoboken, NJ: Wiley, 2007.

[80] J. Oliver, S. Stirling, *Dampness Buildings*, 22 ed. Hoboken, NJ: Wiey, 1997.

[81] E. Taboada, E. Rodriguez, A. Roig, J. Oro, A. Roch, R. Muller "Relaxomatric and Magnetic Characterization of Ultrasmall Iron Oxide Nanoparticles with High Magnetization. Evaluation as Potential T1 Magnetic Resonance Imaging Contrast Agents for Molecular Imaging," *Langmuir,* vol. 23, pp. 4583-4588, 2007.

[82] D. N. Misra, *Absorption on and Surface Chemistry of Hydroxyapatite.* New York: Basic Books, 2004.

[83] K. Tan, P. Cheang, I. A. W. Ho, P. Y. P. Lam, K. M. Hui, "Nanosized bioceramic particles could function as efficient gene delivery vehicles with target specificity for the spleen," *Gene Therapy,* vol. 14, pp. 828-835, 2007.

[84] B. Marquardt, L. Eude, M. Gowtham, G. Cho, H. J. Jeong, M. Chatelet, C. S. Cojocaru, B. S. Kim, D. Pribat, "Density control of electrodeposited Ni nanoparticles/nanowires inside porous anodic alumina templates by an exponential anodization voltage decrease," *Nanotechnology,* vol. 19, pp. 405607-13, 2008.

[85] X. Meng, T. Y. Kwon, Y. Yang, J. L. Ong, K. H. Kim, "Effects of Applied Voltages on Hydroxyapatite Coating of Titanium by Electrophoretic Deposition," *Journal of Biomedical Materials Research,* vol. 78B, pp. 373 - 377, 2005.

[86] R. Folger, L. Weiss, D. Glaves, J. R. Subjeck, J. P. Harlos, "Translational Movements of Macrophages Through Media of Different Viscosities," *Journal of Cell Science,* vol. 31, pp. 245-257, 1978.

[87] J. Narayanan, J. Y. Xiong, X. Y. Liu, "Determination of agarose gel pore size: Absorbance measurements vis a vis other techniques," in *International Conference on Materials for Advanced Technologies.* vol. 28 Singapore: Institute of Physics Publishing, 2006, pp. 83–86.

[88] N. Tandon, C. Cannizzaro, E. Figallo, J. Voldman, G. Vunjak-Novakovic "Characterization of Electrical Stimulation Electrodes for Cardiac Tissue Engineering," in *28th Annual International Conference of the Engineering in Medicine and Biology Society,* New York, NY, 2006, pp. 845-848.

[89] D. Dziong, P. O. Bagnaninchi, R. E. Kearney, M. Tabrizian "Nondestructive Online In Vitro Monitoring of Pre-Osteoblast Cell Proliferation Within Microporous Polymer Scaffolds," *IEEE Transactions on NanoBioscience,* vol. 6, pp. 249-258, 2007.

[90] X. Li, J. Kolega, "Effects of Direct Electric Fields on Cell Migration and Actin Filament Distribution in Bovine Vascular Endothelial Cells," *Journal of Vascular Research,* vol. 39, pp. 391-404, 2002.

[91] A. des Rieux, V. Fievez, M. Garinot, Y. J. Schneider, V. Préat, "Nanoparticles as potential oral delivery systems of proteins and vaccines: a mechanistic approach," *Journal of Controlled Release,* vol. 116, pp. 1-27, 2006.